Computers and Geotechnics 172 (2024) 106482

Contents lists available at ScienceDirect

Computers and Geotechnics

journal homepage: www.elsevier.com/locate/compgeo

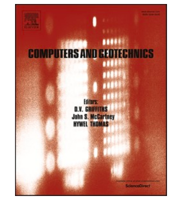

Research Paper

Modeling fluid-driven propagation of 3D complex crossing fractures with the extended finite element method

Fang Shi [a,*], Chunyang Lin [b]

[a] Jiangsu Key Laboratory of Advanced Manufacturing Technology, Huaiyin Institute of Technology, Huai`an 223003, China
[b] Sinopec Petroleum Engineering Technology Research Institute Co., Ltd, Beijing 102200, China

ARTICLE INFO

Keywords:
Extended finite element method
Hydraulic fracturing simulation
Stiffness matrix singularity
Crossing fractures

ABSTRACT

In actual reservoirs, hydraulic fracture networks typically exhibit a complex state characterized by intersecting and non-planar features, posing significant challenges to hydraulic fracturing simulation. In this paper, we present an innovative numerical model based on the extended finite element method (XFEM) for simulating arbitrarily complex intersecting fractures in 3D. For the XFEM simulation of 3D fracture networks, one of the major challenges is the stiffness matrix singularity caused by the complex intersection of fractures. After a detailed discussion of the causes, this paper proposes, for the first time, an efficient and robust strategy to address the stiffness matrix singularity issue, which avoids the need for element subdivision in the integration of enriched elements. A dual-layer Newton-Raphson iteration is established to simulate the fluid–solid coupling process. Besides, a conjugate gradient solver with a Hughes-Winget preconditioner is adopted to solve the discrete linear system of equations using an element-by-element architecture. Another contribution is the proposal of a new algorithm to describe the contact between compressive-shear natural fractures based on the penalty function method. After validating the proposed numerical model, the final example is presented to show its capacity to simulate 3D hydraulic fracturing simulation in which complex crossing fractures are considered.

1. Introduction

Hydraulic fracturing technique is ubiquitous in petroleum engineering and underground engineering, such as reservoir stimulation, geothermal development, and carbon capture and sequestration. The primary purpose of hydraulic fracturing is to inject high-pressure fracturing fluid into the reservoir, creating hydraulic fractures that intersect with existing natural fractures (Chen et al., 2022). This process forms a network of interconnected fractures that serve as high-conductivity pathways for the flow of oil, natural gas, or other fluids, thereby significantly improving energy production efficiency. Due to factors such as the heterogeneities of formations, the complexity of stress fields, the stress shadow effect, and the interaction with natural fractures, hydraulic fractures typically exhibit intricate three-dimensional structures (Abdelaziz et al., 2023) rather than the conventional bi-wing planar fracture patterns. The existence of such non-planar 3D crossing fracture patterns in the subsurface has been widely confirmed by laboratory experiments and field data (Adachi et al., 2007; Jamaloei, 2021; Zhao et al., 2019). Therefore, to gain a more comprehensive understanding of the propagation behavior in naturally fractured rock masses and offer more effective guidance for fracturing design, it is desperately required to conduct in-depth research on complex non-planar 3D scenarios, surpassing the limitations of 2D or basic 3D investigations.

Due to the high cost of experiments and oversimplification of theoretical models, numerical simulation using different methods has proven to be an effective means for hydraulic fracturing investigation (Chen et al., 2022) and has a long history of application since decades ago (Advani and Lee, 1982). A detailed review of numerical models of hydraulic fracturing is out of the scope of this paper and can be found in recently published papers (Chen et al., 2022; Heider, 2021; Jamaloei, 2021; Lecampion et al., 2018; Maulianda et al., 2020). Among these simulation methods, the most commonly used include the finite element method (FEM), the boundary element method (BEM), the discrete element method (DEM), the peridynamics, the phase field model (PFM), the lattice model, the finite volume method (FVM), and the extended/generalized finite element method (XFEM/GFEM). It is worth emphasizing that, in addition to classical simulation methods, there is a promising prospect for the development of coupled methods, such as the hybrid FEM (or XFEM) and peridynamics simulation (Chen et al., 2023; Ni et al., 2020), and the coupled XFEM and phase-field model (Zhang

* Corresponding author.
E-mail address: shifang@hyit.edu.cn (F. Shi).

https://doi.org/10.1016/j.compgeo.2024.106482
Received 5 March 2024; Received in revised form 5 May 2024; Accepted 28 May 2024
Available online 1 June 2024

et al., 2020).

With the advancements in computer hardware capabilities and the gradual maturity of numerical computing technology, there has been an increasing focus on three-dimensional simulation studies compared to two-dimensional ones in recent years. For example, as the earliest adopted method, the FEM was used by Sanchez et al. (2020) to simulate three-dimensional interactions between hydraulic fractures and natural fractures using Abaqus, through which three types of fracture interaction outcomes (crossing, arrested, and opening) were successfully predicted. In their study, the zero-thickness interface elements were utilized to represent fractures, and the behaviors of HFs and NFs were described using the damage constitutive relationship and the Mohr-Coulomb constitutive model, respectively. Tang et al. (2019) employ the displacement discontinuity method (DDM), one of the boundary element methods, to model multiple propagation of HFs in three-dimensional based on the linear elastic fracture mechanics (LEFM) theory. Similarly, Yang et al. (2024) developed a three-dimensional planar model integrating hydraulic fracturing and proppant transport using the DDM. The model was employed for multi-well hydraulic fracturing simulation, considering physical processes such as fluid loss, stress shadow effects, flow distribution along wellbores, perforation-erosion effects, and gravitational settling of proppant. Zhang et al. (2019) developed a fully coupled model based on the synthetic rock mass (SRM) concept initially proposed in the discrete element method and investigated the complex behavior of HFs in fractured rock masses depicted using the discrete fracture network (DFN). Qin and Yang (2023) developed a hydraulic fracturing model based on the peridynamics and investigated the effects of rock mechanical parameters, geostress distribution, and layer dip angle on three-dimensional propagation patterns. As a rapidly developing numerical method, the phase field model has been successfully applied to simulate three-dimensional penny-shaped hydraulic fractures in naturally layered rocks using a staggered scheme to solve the coupled equations (Zhuang et al., 2023). Based on the lattice model, Fu et al. (2019) simulated three-dimensional interactions between HFs and NFs using a commercial software Xsite. In their simulation, 2D interaction scenarios including stopped, crossing, and crossing with offset were extended to 3D and then successfully implemented to simulate three-dimensional intersecting fractures. Zheng et al. (2019) proposed a FVM-based model to perform 3D planar hydraulic fracturing simulation in which the Barton-Bandis contact model (Bandis et al., 1983) was used to simulate fracture closure and avoid non-physical results. In addition, Shauer and Duarte (2022) proposed a GFEM-based 3D methodology to simulate the propagation and interaction between HFs inside which the fluid flow is assumed to follow the Reynolds lubrication theory. It is worth noting that, although some advancements have been made in three-dimensional simulations, there is still limited progress in complex simulations involving the interactions between HFs and NFs.

The XFEM proposed by Professor Belytschko (Belytschko and Black, 1999) has been adopted as a popular numerical method to perform hydraulic fracturing simulation for more than 15 years (Lecampion, 2009). Unlike traditional finite element methods, the XFEM (Khoei, 2015) captures fracture deformations by introducing the partition of unity functions (Moës et al., 1999). By adding extra degrees of freedom (DOFs) for the elements penetrated by fractures and introducing enrichment functions to the FEM formulation, fractures can propagate autonomously regardless of the underlying mesh structure. Thus, the need for remeshing, mesh refinement, and associated data mapping between meshes can be fundamentally avoided. By introducing junction enrichment functions (Cruz et al., 2018), complex intersecting fractures can be conveniently and accurately simulated. In recent years, two-dimensional hydraulic fracturing simulation based on the XFEM has gradually matured, with extensive research being conducted on topics such as interaction with natural fractures (Taleghani and Olson, 2014; Khoei et al., 2016; Vahab et al., 2019) and caves (Cheng et al., 2019), contact formulation (Hirmand et al., 2015), proppant transport (Hosseini and Khoei, 2020), porous media (Khoei and Haghighat, 2011), fluid leak-off (Jafari et al., 2021), heterogeneous reservoir (Jin and Arson, 2020), multi-field coupling (Luo et al., 2022), and dynamic simulation (Parchei-Esfahani et al., 2020). However, there are only a few studies available when it comes to 3D hydraulic fracturing simulation using the XFEM framework. Among these studies, Paul et al. (2018) introduced a fully coupled numerical approach to simulate the reorientation of a single 3D fluid-driven fracture in a poroelastic reservoir using the XFEM. Roth et al. (2020a, 2020b) established an XFEM formulation for simulating the non-planar hydraulic fracture in concrete dams. Wang et al. (2020) presented an XFEM-based model for 3D propagation processes of planar fluid-driven fracture. Recently, the authors (Shi and Liu, 2021) introduced a fully coupled 3D numerical model for non-planar hydraulic fracturing simulation within the framework of XFEM. Based on our proposed model, an in-depth investigation into the phenomenon of fracture front segmentation was conducted (Shi et al., 2022a; Shi et al., 2022b). As a method similar to the XFEM, the GFEM is being gradually adopted by some researchers for 3D hydraulic fracturing simulation and some advances have been made (Gupta and Duarte, 2018; Mukhtar et al., 2022; Shauer and Duarte, 2022). However, to the best of our knowledge, research on three-dimensional intersecting fractures using either XFEM or GFEM remains exceedingly scarce. Due to the advantages and potential of the XFEM, some commercial software packages have developed XFEM capabilities, and the typical representative is Abaqus (Dehghan et al., 2017; Haddad and Sepehrnoori, 2016). However, Abaqus still has significant limitations when it comes to the simulation of interactions between HFs and NFs, especially under 3D conditions. The main challenges lie in accurately describing and tracking 3D complex fractures and resultant network, as well as effectively addressing a series of enrichment-related issues, such as the identification of enriched elements and nodes, the numerical integration, the high condition number of the stiffness caused by additional DOFs, and other considerations (Shi and Liu, 2021).

This article summarizes the recent progress we have made in 3D simulation of complex fluid-driven fracture propagation using the XFEM and focuses on simulating intersecting fractures rather than the fluid–solid coupling strategy. It should be noted that the fluid flow inside the fractures and fluid exchange between the fluid inside the fracture and the porous matrix could affect the whole hydraulic fracturing process, especially in the time steps when the fractures cross (Khoei et al., 2018). However, for the sake of brevity and clarity, the uniform fluid pressure within the hydraulic fracture in an impermeable linear elastic medium is assumed in this paper. As a result, the proposed model is only applicable for fracturing with extremely low-viscosity fluid. In addition, proppant-related issues, the fluid lag near the fracture tip, the body force, and the dynamic effects of fracture propagation are also neglected. It should be noted that all these assumptions will not limit the applicability of the proposed methodology.

This paper is organized as follows. Firstly, the strong, weak, and discretized forms of the governing equation are briefly presented in Section 2. Section 3 delves into various aspects of algorithms employed for the computational implementation. Model verification is given in Section 4 in which the final example is presented to demonstrate the model's capability in handling large-scale intersecting fractures. Section 5 presents the concluding remarks.

2. Governing equation

As shown in Fig. 1, a three-dimensional domain Ω with boundary Γ contains an evolving hydraulic fracture (denoted by *HF*) Γ_{HF} and a frictional fracture (denoted by *FF*) Γ_{FF}, whose faces are distinguished using signs $(+)$ and $(-)$. The boundaries of applied external force $\bar{\mathbf{t}}$ and displacement $\bar{\mathbf{u}}$ of the domain Ω are represented by Γ_t and Γ_u, respectively. The outwards normal vector of the negative side $(-)$ of Γ_{HF} and Γ_{FF} are $\mathbf{n}_{\Gamma_{HF}}$ and $\mathbf{n}_{\Gamma_{FF}}$, respectively. Besides, an incompressible Newtonian fluid is pumped into the HF at a rate of Q_{inj}.

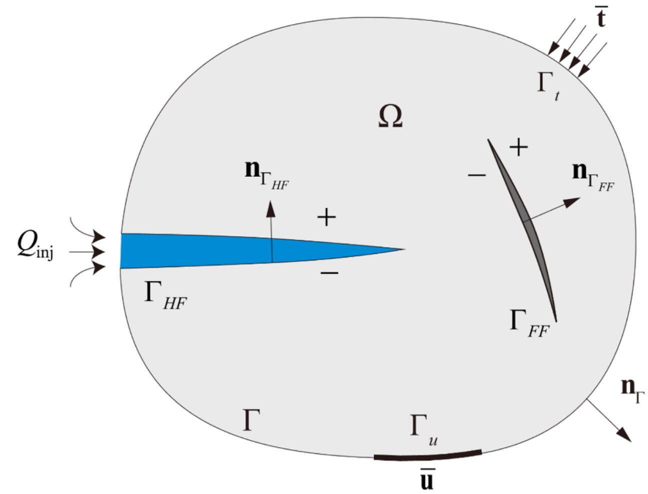

Fig. 1. Schematic of a 3D domain with a hydraulic fracture and a frictional fracture.

2.1. Momentum balance equation

In this paper, the momentum balance equation is used to capture the mechanical deformation of rock media:

$$\nabla\cdot\boldsymbol{\sigma} = 0 \qquad in \quad \Omega \tag{1}$$

and the corresponding boundary conditions can be written as:

$$\begin{cases} \mathbf{u} = \bar{\mathbf{u}} & on\,\Gamma_u \\ \boldsymbol{\sigma}\cdot\mathbf{n}_{\Gamma_t} = \bar{\mathbf{t}} & on\,\Gamma_t \\ \boldsymbol{\sigma}\cdot\mathbf{n}_{\Gamma_{HF}} = \mathbf{t}^{\text{cont}} + p\mathbf{n}_{\Gamma_{HF}} & on\,\Gamma_{HF} \\ \boldsymbol{\sigma}\cdot\mathbf{n}_{\Gamma_{FF}} = \mathbf{t}^{\text{cont}} + p\mathbf{n}_{\Gamma_{FF}} & on\,\Gamma_{FF} \end{cases} \tag{2}$$

where $\boldsymbol{\sigma}$ represents the Cauchy stress tensor, $\mathbf{t}^{\text{cont}}$ denotes the contact force acting between surfaces of frictional fractures or the closed part of hydraulic fractures, and p represents the fluid pressure acting on the surfaces of the hydraulic fractures or the natural fractures partially filled with fluid when crossed by a hydraulic fracture. Besides, the deformation of the reservoir follows a linear elastic constitutive relationship:

$$\boldsymbol{\sigma} = \mathbf{D} : \boldsymbol{\varepsilon} \tag{3}$$

where $\mathbf{D}$ is the elastic matrix, and $\boldsymbol{\varepsilon}$ represents the small strain tensor.

2.2. Weak form and XFEM discretization

After introducing the trial function $\mathbf{u}(\mathbf{x}, t)$ and test function $\delta\mathbf{u}(\mathbf{x}, t)$, the weak form of the equilibrium equation can be obtained (Khoei et al., 2015):

$$\int_{\Omega}\delta\boldsymbol{\varepsilon} : \boldsymbol{\sigma} d\Omega + \int_{\Gamma_{HF}}[[\delta\mathbf{u}]]\cdot p\mathbf{n}_{\Gamma_{HF}} d\Gamma + \int_{\Gamma_{FF}}[[\delta\mathbf{u}]]\cdot\mathbf{t}^{\text{cont}} d\Gamma = \int_{\Gamma_t}\delta\mathbf{u}\cdot\mathbf{t} d\Gamma \tag{4}$$

In this equation, the double bracket symbol $[[\delta\mathbf{u}]]$ represents the jump of $\delta\mathbf{u}$ between faces "+" and "−", that is, $[[\delta\mathbf{u}]] = \delta\mathbf{u}(\Gamma^+) - \delta\mathbf{u}(\Gamma^-)$.

Within the framework of XFEM, for a given point $\mathbf{x}$, its displacement $\mathbf{u}(\mathbf{x})$ can be expressed as (Shi et al., 2017):

$$\mathbf{u}(\mathbf{x}) = \sum_{I\in S_{all}} N_I(\mathbf{x})\mathbf{u}_I + \sum_{I\in S_H} N_I(\mathbf{x})H(\mathbf{x})\mathbf{a}_I + \sum_{I\in S_{tip}} N_I(\mathbf{x})\sum_{l=1}^{4} F_l(\mathbf{x})\mathbf{b}_I^l + \sum_{I\in S_J} N_I(\mathbf{x})J(\mathbf{x})\mathbf{c}_I \tag{5}$$

where N_I is the conventional shape function of node I, $\mathbf{u}_I$ denotes the conventional displacement vector, $H(\mathbf{x})$ represents the Heaviside enrichment function related to enriched DOF vector $\mathbf{a}_I$, $F(\mathbf{x})$ denotes the tip enrichment function associated with enriched DOF vector $\mathbf{b}_I$, and $J(\mathbf{x})$ represents the junction enrichment function related to enriched DOF vector $\mathbf{c}_I$. In addition, the letter 'S' is short for set, and S_{all}, S_H, S_{tip}, and S_J denote the sets of all nodes in the model, the Heaviside enrichment nodes, the tip enrichment nodes, and the junction enrichment nodes, respectively.

The Heaviside enrichment function for the strong discontinuity of fractures is defined as

$$H(\mathbf{x}) = \begin{cases} 1 & if \quad (\mathbf{x}-\mathbf{x}^*)\cdot\mathbf{n}_{\Gamma_F} \geqslant 0 \\ -1 & otherwise \end{cases} \tag{6}$$

in which the symbol $\mathbf{x}^*$ represents the point on the fracture surface closest to point $\mathbf{x}$. Using the analytical solution derived from the displacement field near the fracture tip in brittle materials, the expression of the tip enrichment function can be written as:

$$\{F_l(r,\theta)\}_{l=1,\ldots,4} = \left\{\sqrt{r}\sin\frac{\theta}{2}, \sqrt{r}\cos\frac{\theta}{2}, \sqrt{r}\sin\theta\sin\frac{\theta}{2}, \sqrt{r}\sin\theta\cos\frac{\theta}{2}\right\} \tag{7}$$

where r and θ are coordinate components of the local cylindrical coordinate system oriented along the fracture front (Shi and Liu, 2021).

In this study, the junction enrichment function (Daux et al., 2000) is adopted to consider the T-shaped, cross-shaped, and more complex intersecting fractures. As shown in Fig. 2 (a) (It should be noted that, to facilitate a clearer illustration, Figs. 2–4 in this paper are presented in a two-dimensional form.), V^+ and V^- are subregions divided by the main fracture M. Then, $J(\mathbf{x})$ takes the value of 0 for a point $\mathbf{x}$ in region V^+. As depicted in Fig. 2 (b), for a point $\mathbf{x}$ in region V^-, $J(\mathbf{x})$ equals either 1 or -1 depending on its position relative to the minor fracture m. According to this rule, the junction enrichment function can be expressed as:

$$J(\mathbf{x}) = \begin{cases} H^m(\mathbf{x}) & if\, H^M(\mathbf{x}) \leqslant 0 \\ 0 & otherwise \end{cases} \tag{8}$$

where $H^M(\mathbf{x})$ and $H^m(\mathbf{x})$ denote the Heaviside enrichment functions associated with fractures M and m, respectively.

For cross-shaped or more complex intersecting fractures, a feasible approach is to decompose the complex intersecting fractures into several combinations of T-shaped intersecting fractures. As a typical example, the strategy for selecting enriched nodes for the cross-shaped fractures is depicted in Fig. 3 (a). In this example, two sets of T-shaped intersecting fractures can be found, namely, the master fracture AB and minor fracture OD (labeled as AB-OD) as one set, and AB and OC (labeled as AB-OC) as another set. Therefore, nodes of the element containing the intersection point O should be enriched with two sets of junction enrichment functions, representing the branches OD and OC, respectively. For more complex intersecting fractures, take the snowflake-shaped case given in Fig. 3 (b) for example, point O should be

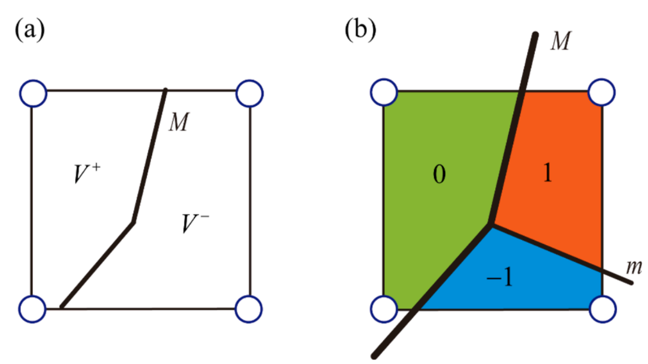

Fig. 2. A schematic diagram illustrating the junction enrichment function. (a) The element is partitioned into two regions, V^+ and V^-, by the main fracture M; (b) The values of the junction enrichment function. The hollow circles represent the nodes of the element.

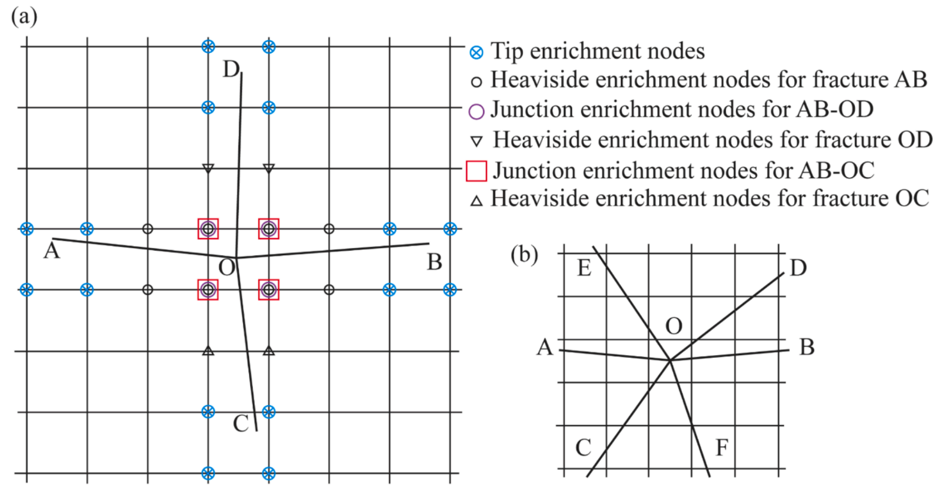

Fig. 3. Illustration of node enrichment scheme. (a) Cross-shaped intersecting fractures and (b) snowflake-shaped intersecting fractures.

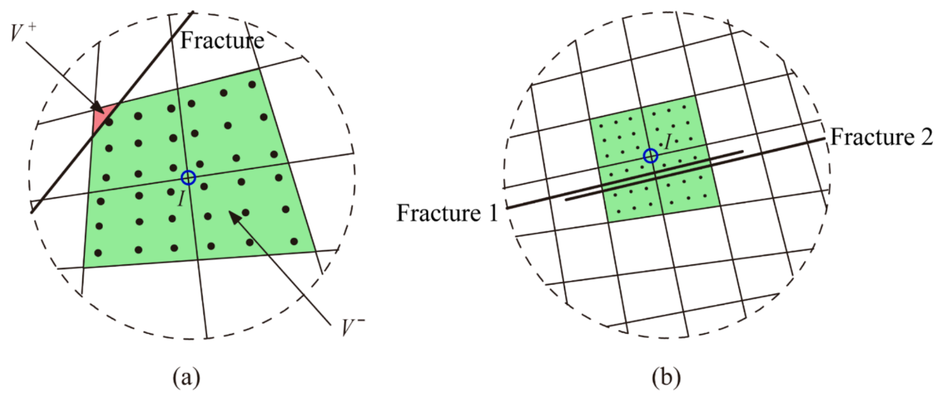

Fig. 4. A schematic diagram illustrating situations that lead to a singular stiffness matrix. (a) The support domain of node I composed of V^+(colored in red) and V^-(colored in green) cut through by a fracture; (b) Two fractures are partially overlapped with a small gap. The black dots represent integration points. The blue circle represents node I. The integration points are used for illustration purposes only and do not represent the actual number of integration points adopted in this paper.

enriched with four sets of junction enrichment functions. As a final note, it is worth mentioning that the treatment of blending elements is necessary to maintain the partition of unity property and details can be found in the referenced paper (Shi et al., 2022a).

After substituting the Eq. (5) to Eq. (4), we can derive the discretized form of the balance equation:

$$\mathbf{KU} - \mathbf{QP} - \mathbf{F}^{\mathrm{ext}} = \mathbf{0} \tag{9}$$

where $\mathbf{K}$ is the global stiffness matrix that takes into account the contact effect between the fracture surfaces (Shi et al., 2017); $\mathbf{U}$ represents the unknown global displacement vector to be solved, which includes both the conventional DOFs and the enriched DOFs; $\mathbf{Q}$ is the fluid–structure coupling matrix (Shi and Liu, 2021) that converts the fluid pressure into equivalent nodal loads acting on enriched nodes; $\mathbf{P}$ denotes the global vector of fluid pressure; and $\mathbf{F}^{\mathrm{ext}}$ is the global external force vector.

3. Computational implementation

In this section, we will discuss details on the numerical implementation of complex intersecting fracture simulation within the framework of the XFEM. Firstly, in Section 3.1, we will investigate the causes of stiffness matrix singularity arising from complex intersecting fractures and propose a solution in Section 3.2. On account of the ubiquitous existence of natural fractures in reservoirs, Section 3.3 presents a penalty function-based approach for efficiently simulating natural fractures. The fracture propagation criteria and the smooth algorithm for the fracture front will be presented in Section 3.4. Section 3.5 introduces a dual-layer Newton-Raphson iterative scheme to solve the proposed model. Finally, a linear equation system solver based on the element-by-element (EBE) scheme and the Hughes-Winget (HW) preprocessor will be discussed in Section 3.6. For additional details that have not been covered in this paper, readers are referred to our previous work (Shi and Liu, 2021; Shi et al., 2022b; Shi et al., 2017).

3.1. Challenges of stiffness matrix singularity

In the XFEM, the numerical integration of enriched elements intersected by fractures occupies a position of great importance. Inappropriate integration can result in stiffness matrices with tiny eigenvalues (high condition numbers), leading to difficulties in solving the linear equation system. Here, we provide two examples to illustrate this issue. Firstly, consider the situation shown in Fig. 4 (a), where the support domain of node I is divided into two parts V^+ and V^- by a fracture surface. However, in this example, the V^+ colored in red does not contain any Gaussian integration points. When assembling the global stiffness matrix for Heaviside enrichment elements, the derivative matrix $\mathbf{B}$ of shape functions needs to be computed according to the following equation:

$$\mathbf{B}_I^{\mathbf{a}} = \begin{bmatrix} \frac{\partial N_I^H}{\partial x} & 0 & 0 & \frac{\partial N_I^H}{\partial y} & 0 & \frac{\partial N_I^H}{\partial z} \\ 0 & \frac{\partial N_I^H}{\partial y} & 0 & \frac{\partial N_I^H}{\partial x} & \frac{\partial N_I^H}{\partial z} & 0 \\ 0 & 0 & \frac{\partial N_I^H}{\partial z} & 0 & \frac{\partial N_I^H}{\partial y} & \frac{\partial N_I^H}{\partial x} \end{bmatrix}^{\mathrm{T}} \tag{10}$$

in which

$$N_I^H = N_I(H(\mathbf{x}_G) - H(\mathbf{x}_I)) \tag{11}$$

In Eq. (11), $\mathbf{x}_G$ and $\mathbf{x}_I$ denote the Gaussian integration point and node I, respectively. From this equation, it can be inferred that the resulting matrix $\mathbf{B}_I^{\mathbf{a}}$ is empty since all Gaussian integration points possess the same Heaviside function value with node I. Therefore, from the perspective of linear algebra, the resultant global stiffness matrix will have identical rows and zero determinant, indicating that the linear equation system is unsolvable. Additionally, if V^+ contains only a very small number of Gaussian points, it will not cause the zero determinant of stiffness matrix, but it will still lead to a large condition number of the stiffness matrix, potentially resulting in an ill-conditioned system of equations. Unfortunately, this problem cannot be fundamentally solved by improving the integration accuracy through methods such as subdivision into sub-tetrahedral elements (Shi and Liu, 2021).

Another example is shown in Fig. 4 (b), in which two parallel fractures are partially overlapped with a small gap. Taking node I as an example, it is evident that this node should be selected as a Heaviside enrichment node for both fracture 1 and fracture 2, labeled as H_{F1} and H_{F2}, respectively. Obviously, the contributions of enrichment nodes H_{F1} and H_{F2} to the global stiffness matrix are exactly the same. As a result, the stiffness matrix will unavoidably have identical rows and possess singular characteristics.

3.2. Integration strategy for the enriched elements

From a mathematical perspective, the approach to solving this problem stated in the preceding Section 3.1 is straightforward: simply delete duplicate rows or approximately identical rows of the stiffness matrix. From a numerical implementation perspective, this means removing redundant enriched nodes. In this study, the scheme to delete redundant enriched nodes is related to the integration strategy proposed based on the standard Gauss integration.

This paper uses 8-node hexahedral elements to mesh the computational domain. For 8-node hexahedral elements without enrichment nodes, the blending elements, and the enriched elements, $2 \times 2 \times 2$, $6 \times 6 \times 6$, and $8 \times 8 \times 8$ integration points are respectively used to perform the standard Gauss integration. For enriched elements related to two or more fractures, $10 \times 10 \times 10$ integration points are adopted. Let's denote the total number of integration points in enriched elements within the support domain of node I as n_G. Once a Heaviside enrichment node I is preliminarily determined for a fracture C, the program will loop through all these n_G Gaussian integration points, and count the number of integration points with positive and negative Heaviside function values relative to fracture C and mark with n_V^+ and n_V^-, respectively. In this step, the method to calculate the signed distance from a point to a fracture surface explicitly represented by spatial triangle patches has been given in detail in our recent study (Shi and Liu, 2021). Afterwards, if n_V^+/n_G or n_V^-/n_G is less than a threshold value, then the Heaviside enrichment node of fracture C should be removed. After conducting numerous numerical experiments involving complex intersecting cracks, it was found that the integration strategy exhibits high robustness by taking the threshold value as 5 %.

For the second scenario in Fig. 4 (b), the paper introduces an integer string to identify and then remove redundant Heaviside enhancement nodes corresponding to overlapping fractures. For a fracture C, its integer string C_{string} used to mark the position relative to the 8 nodes of an element can be calculated according to the following formula:

$$C_{string} = \sum_{i=1}^{8} 10^{i-1} H_{node\_i} \tag{12}$$

where H_{node_i} represents the Heaviside function of node i relative to fracture C. Form Eq. (12) it can be seen that there are a total of 256 (i.e., 2^8) possible position configurations. According to this equation, it is laconic and convenient to numerically determine the relative orientation of the fracture surfaces inside elements. For example, the integer strings of fracture 1 and fracture 2 shown in Fig. 5 can be easily calculated as 11,108,889 and 11,111,089, respectively. If identical or opposite integer strings exist within an element, then these fractures might be overlapping and further evaluation of the Gaussian points between the two cracks is necessary. If no Gaussian points exist between cracks, redundant Heaviside enrichment nodes should be removed. Afterwards, the signed distance should be calculated according to an offset crack position which is taken as the middle position of the overlapping cracks.

Since this paper utilizes OpenMP for parallel computing, this algorithm can be executed with very high efficiency. Extensive computations have shown that this method can significantly reduce the condition number of the stiffness matrix, effectively alleviating the ill-conditioning of the system of linear equations. Furthermore, this method can avoid the extremely challenging task of tetrahedron partitioning for complex intersecting fractures. The method is concise enough, possesses strong robustness, and is therefore chosen as the integration strategy to handle complex intersecting fractures in this paper.

3.3. Novel contact algorithm for compressive-shear natural fractures

Reservoirs typically contain countless natural fractures. In the hydraulic fracturing simulation, if all natural fractures are treated as frictional fracture surfaces and participate in the contact iteration calculation (Shi et al., 2017), the overall computational cost would be unbearable. In reality, NFs far from HFs have limited influence on the growth of HFs. This paper utilizes the penalty function method (Chandrupatla et al., 2012) to dexterously link the x, y, z components of enriched degrees of freedom and the l, m, n components of the normal vector $\mathbf{n}$ of fracture surface, thereby constraining the normal displacement and simulating the contact sliding process of the fracture plane. This approach does not require the contact iteration process, thus effectively improving the efficiency of large-scale hydraulic fracturing simulation.

Let's denote the displacement components of the enriched node as $\mathbf{u} = (u_x, u_y, u_z)$, and denote the normal vector of the fracture plane as $\mathbf{n} = (l, m, n)$. As shown in Fig. 6, if the fracture is a shear-type natural fracture, the fracture plane allows only tangential sliding without normal displacement. The displacement vector of the enriched nodes must lie within the fracture plane. Therefore, from a 3D geometrical point of view, the components of the enriched degrees of freedom (x, y, z) and the components of the fracture normal vector (l, m, n) should satisfy the following constraint relationship:

$$lu_x + mu_y + nu_z = 0 \tag{13}$$

The above equation represents a system of multiple constraints, which can be handled within the framework of the finite element method using the penalty function approach. Hence, the modification of the stiffness matrix can be carried out according to the following equation:

$$\begin{bmatrix} k_{xx} & k_{xy} & k_{xz} \\ k_{yx} & k_{yy} & k_{yz} \\ k_{zx} & k_{zy} & k_{zz} \end{bmatrix} \rightarrow \begin{bmatrix} k_{xx} + l^2\chi & k_{xy} + lm\chi & k_{xz} + ln\chi \\ k_{yx} + ml\chi & k_{yy} + m^2\chi & k_{yz} + mn\chi \\ k_{zx} + nl\chi & k_{zy} + nm\chi & k_{zz} + n^2\chi \end{bmatrix} \tag{14}$$

In the above formula, k_{ij} is the component of the element stiffness matrix, and χ is the penalty parameter, which takes the value of $1.0 \times$

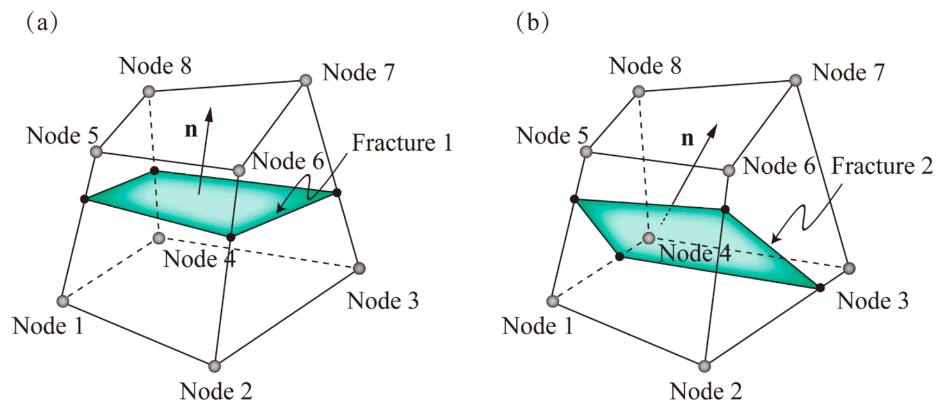

Fig. 5. Illustration for the calculation of integer string to identify overlapping fractures. (a) The integer string for fracture 1 is 11,108,889 and (b) the integer string for fracture 2 is 11,111,089. n represents the normal vector of fracture surfaces.

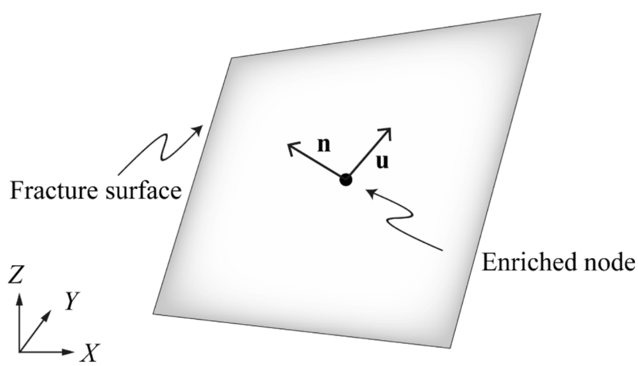

Fig. 6. Displacement vector u of an enriched node for a shear-type pre-existing natural fracture.

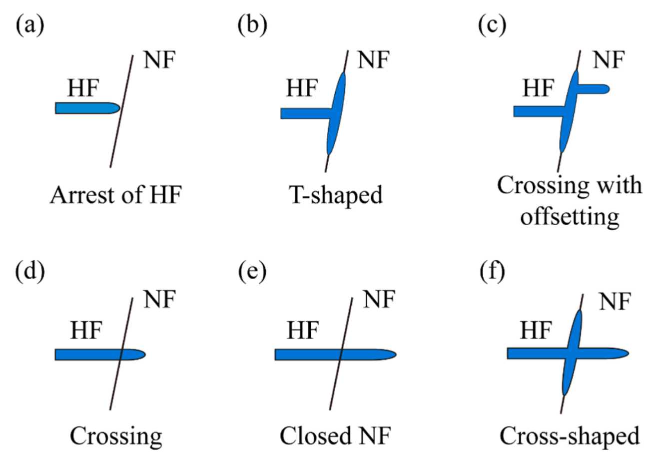

Fig. 7. Illustration of potential interaction situations between a hydraulic fracture and a pre-existing natural fracture.

10^{12} N/m in this study. Verification of the proposed contact algorithm will be presented in Section 4.3. It should be noted that the proposed contact algorithm only allows a frictionless slide between the fracture faces and will restrict fracture opening as well. In this paper, this algorithm is adopted only for natural fractures far from the hydraulic fractures. For natural fractures approached to or intersected by hydraulic fractures, the contact iteration calculation is performed according to the penalty method (Khoei, 2015).

3.4. Fracture propagation model

The fracture propagation model consists of three aspects: the fracture propagation criteria, the fracture interaction criteria, and the smoothing algorithm for fracture fronts. In this paper, as described in our previous work (Shi and Liu, 2021), Schöllmann's criterion (Schöllmann et al., 2002), alongside a displacement extrapolation method to calculate stress intensity factors, is employed to ascertain the timing and manner in which fracture propagation occurs. The interactions between NFs and NFs are the main cause of the formation of complex fracture networks. Therefore, it is necessary to address possible interaction modes between HFs and NFs.

When a HF approaches a NF, several scenarios can typically happen depending mainly on the in-situ stress, fluid pressure within the fracture, and the approaching angle. As shown in Fig. 7 (a), the HF can be arrested if the hydraulic fluid pressure is below the normal compressive stress acting on the HF. Conversely, when hydraulic fluid pressure surpasses the normal compressive stress, the HF will cross the NF, as depicted in Fig. 7 (d). In both scenarios, if the shear stress of the NF reaches its stress strength, slippage occurs between NF surfaces. In the case of the former scenario (Fig. 7 (a)), if the hydraulic fluid pressure continues to rise and exceeds the normal compressive stress acting on the NF, it leads to the opening and dilation of the NF, forming a T-shaped junction, as shown in Fig. 7 (b). During the opening process of the NF, the HF can be offset if the stress exceeds the tensile strength of rock matrix, as shown in Fig. 7 (c). For the scenario illustrated in Fig. 7 (d), if the NF experiences significant compressive stress, the HF will continue to propagate while the NF remains closed, as shown in Fig. 7 (e). However, if the hydraulic fracture pressure exceeds the normal compressive stress acting on the natural fracture, the natural fracture can then be opened, resulting in the formation of cross-shaped intersecting fractures, as shown in Fig. 7 (f). Although the interaction between HFs and NFs is of great importance for hydraulic fracturing simulations, it is not the focus of this paper. Readers can refer to the work of other researchers (Fu et al., 2019; Sanchez et al., 2020; Taleghani et al., 2016) for a more in-depth insight into the interaction mechanisms between HFs and NFs.

The activation and slippage of NFs are determined according to the Mohr-Coulomb model (Sanchez et al., 2020). For a stress state $\boldsymbol{\sigma}$ between fracture surfaces, slippage happens if the following equation is satisfied:

$$f(\boldsymbol{\sigma}) = \sqrt{\tau_s^2 + \tau_t^2} - c + \sigma_n \tan(\phi_f) > 0 \quad (15)$$

where τ_s and τ_t are the shear stresses on natural fracture surfaces and σ_n represents the corresponding effective normal stress; c and ϕ_f are the cohesion and the internal friction angle of NFs, respectively.

In this study, the fracture surfaces are composed of spatial triangles (Shi and Liu, 2021). As the fracture surface expands, the position of the fracture front continuously changes. If the propagation increment of a fracture front is smaller than $0.2l_c$ (l_c represents the characteristic length and can be obtained by $l_c = \overline{V}_{enrich}^{1/3}$, where $\overline{V}_{enrich}$ denotes the average volume of all enriched elements), only the position of the fracture front needs to be updated, while the topological relationships of triangles associated with that fracture front remain unchanged. For example, in Fig. 8, the fracture front vertex 2 was updated to point 2^{New}, and no new triangles were generated during the updating process. However, if the propagation increment of the fracture front exceeds $0.2l_c$, new triangle triangles should be added to ensure the accuracy of explicit fracture surface description. For instance, in Fig. 8, the fracture front vertex 4 propagates to vertex 16, resulting in the addition of triangles △3-4-16 and △4-5-16. Moreover, if the length of the propagated fracture front line exceeds $2l_c$, a new triangle point needs to be added at the midpoint of that fracture front boundary. For example, as can be seen in Fig. 8, a new vertex 19 was added to line 17–18.

To improve the smoothness of the fracture surface, it is necessary to further smooth the updated fracture front (e.g., the fracture front 8-17-19-18-5-16-3-2^{New}-11-10-9 shown in Fig. 8). In this paper, the Taubin algorithm (Taubin, 1995) is used to perform the smoothing procedure. Assuming that the fracture front is comprised of n points connected end-to-end ($\mathbf{p}_1$, $\mathbf{p}_2$, …, $\mathbf{p}_n$), the Taubin smoothing algorithm reads:

$$\begin{aligned} \mathbf{p}'_i &= \mathbf{p}_i + \lambda L(\mathbf{p}_i) \\ \mathbf{p}''_i &= \mathbf{p}'_i - \mu L(\mathbf{p}'_i) \end{aligned} \tag{16}$$

where λ and μ are the Taubin smoothing coefficients, and are taken as 0.33 and 0.331, respectively in this paper; $L(\mathbf{p}_i)$ is iteratively calculated according to the following formula:

$$L(\mathbf{p}_i) = \frac{w_{ij}\mathbf{p}_j + w_{ik}\mathbf{p}_k}{w_{ij} + w_{ik}} - \mathbf{p}_i \tag{17}$$

where $\mathbf{p}_j$ represents the previous point adjacent to point $\mathbf{p}_i$, and $\mathbf{p}_k$ represents the next point adjacent to point $\mathbf{p}_i$. $w_{ij} = 1/l_{ij}$, and $w_{ik} = 1/l_{ik}$, where l_{ij} is the distance between points $\mathbf{p}_i$ and $\mathbf{p}_j$.

3.5. Dual-layer Newton-Raphson iteration

During the fluid–structure coupling calculation of hydraulic fracturing, it is necessary to ensure that each propagation step satisfies the quasi-static fracture propagation criterion. Moreover, mass conservation needs to be maintained during the propagation process. This implies that, without considering fluid loss, the volume of the hydraulic fractures should be equal to the injected fluid volume. As a result, from a global perspective, the calculation process involves two levels of iterative computations. In this paper, a dual-layer Newton-Raphson iteration is introduced for solving the fluid–structure coupling problem, as shown in Fig. 9.

The outer Newton-Raphson iteration is used to adjust the time step to ensure that the quasi-static fracture propagation criterion is satisfied:

$$\left(K_{eq}^{\max}\right)_j^{n+1} \in \left[(1-\alpha)K_{IC},\ \ (1+\alpha)K_{IC}\ \right] \tag{18}$$

Here, n represents the time step, and j represents the fluid pressure iteration step. K_{IC} is the fracture toughness, α is a coefficient of value 0.05, and $K_{eq}^{\max}$ is the maximum equivalent stress intensity factor at the fracture front (Shi and Liu, 2021). Typically, the outer Newton-Raphson iteration converges within 2–3 iterations. The inner Newton-Raphson iteration is used to adjust the fracturing fluid pressure to fulfill mass conservation law.

$$\left(\sum_i A_i w_i^{n+1}\right)_j - \left(\sum_i A_i w_i^{n}\right)_j = q^{n+1}(\Delta t)_j \tag{19}$$

where, i represents the fluid element number, A_i and w_i denote the area and the average aperture of the i-th fluid element, respectively. q represents the injection flow rate, and Δt represents the time step increment. Typically, the inner Newton-Raphson iteration converges within 3 iterations. It should be noted that the contact or sliding state of fracture surfaces is detected within the inner iteration.

In the above dual iterative process, the stiffness matrices for the conventional FEM elements, which constitute the major part, only need to be computed once. The element stiffness matrices related to XFEM elements, on the other hand, need to be dynamically added or updated after fracture propagation. Due to the symmetry of the stiffness matrix, it is sufficient to store only the upper triangular part to reduce memory

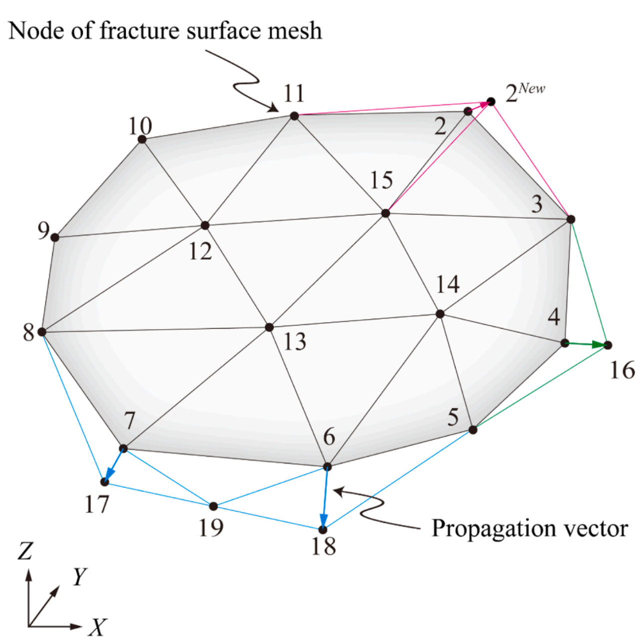

Fig. 8. Diagram of fracture surface updating algorithm.

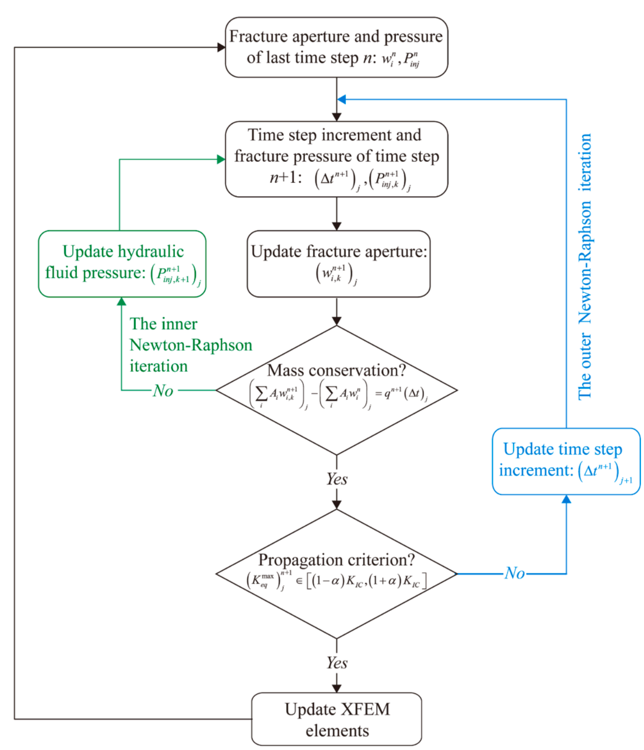

Fig. 9. Flowchart of the two-level Newton-Raphson iteration for the fluid–structure coupling problem.

consumption. Besides, since the Fortran programming language adopted in this study does not possess automatic array expansion capabilities, a ragged array class has been developed based on object-oriented techniques to store variables related to element stiffness matrices of XFEM elements. This class can automatically expand the dimensions of relevant arrays as fracture propagates, thereby accommodating various scales of three-dimensional hydraulic fracturing simulations without pre-allocating memory.

3.6. Linear equation solver

By incorporating the element-by-element approach on top of the conjugate gradient method, it is possible to avoid assembling the global stiffness matrix. This approach is particularly suited for large-scale three-dimensional analyses as it dramatically reduces the memory requirements (Gullerud and Dodds, 2001). This approach not only simplifies the implementation but also facilitates efficient parallel computing using OpenMP.

Let's express Eq. (9) in a more general form $\mathbf{KU} = \mathbf{F}$, and then introduce a preconditioning matrix $\mathbf{C}$, then its residual can be written as

$$\overline{\mathbf{R}}_0 = \mathbf{p}_0 = \mathbf{C}^{-1}\mathbf{R}_0 = \mathbf{C}^{-1}(\mathbf{F} - \mathbf{K}\mathbf{U}_0) \tag{20}$$

where $\mathbf{U}_0$ is the initial guess of the displacement field, and $\mathbf{p}$ is an intermediate variable in the iterative solution process. For the k-th iteration step, the EBE iterative calculation process is as follows (Smith et al., 2014):

$$\begin{cases} \alpha_k = \mathbf{R}_k^{\mathrm{T}}\overline{\mathbf{R}}_k / \left(\mathbf{p}_k^{\mathrm{T}}\mathbf{K}\mathbf{p}_k\right) \\ \mathbf{U}_{k+1} = \mathbf{U}_k + \alpha_k \mathbf{p}_k \\ \mathbf{R}_{k+1} = \mathbf{R}_k - \alpha_k \mathbf{K}\mathbf{p}_k \\ \overline{\mathbf{R}}_{k+1} = \mathbf{C}^{-1}\mathbf{U}_{k+1} \\ \beta_k = \mathbf{R}_{k+1}^{\mathrm{T}}\overline{\mathbf{R}}_{k+1} / \mathbf{R}_k^{\mathrm{T}}\overline{\mathbf{R}}_k \\ \mathbf{p}_{k+1} = \overline{\mathbf{R}}_{k+1} + \beta_k \mathbf{p}_k \end{cases} \tag{21}$$

where α defines the step size, $\mathbf{U}_{k+1}$ is the updated displacement, β represents the correction factor, and $\mathbf{p}$ defines the step direction. The solution converges when the following criterion is satisfied:

$$\|\mathbf{U}_{k+1} - \mathbf{U}_k\| / \|\mathbf{U}_k\| \leqslant \varepsilon_{Tol} \tag{22}$$

where the tolerance ε_{Tol} is taken as 1.0×10^{-6} in this paper.

In this paper, the Hughes-Winget (HW) preconditioner is adopted to accelerate the iterative calculation. Therefore, the preconditioning matrix $\mathbf{C}$ can be written as

$$\mathbf{C} = \mathbf{D}_s^{1/2}\left(\prod_{e=1}^{N_{elem}} \overline{\mathbf{L}}_e \prod_{e=1}^{N_{elem}} \overline{\mathbf{D}}_e \prod_{e=N_{elem}}^{1} \overline{\mathbf{L}}_e^{\mathrm{T}}\right)\mathbf{D}_s^{1/2} \tag{23}$$

Here, $\mathbf{D}_s$ and $\mathbf{D}_e$ are the diagonal matrices of $\mathbf{K}$ and of element stiffness matrix $\mathbf{K}_e$, respectively; $\overline{\mathbf{L}}_e$ represents the Crout factor of matrix $\mathbf{I} + \mathbf{D}_e^{-1/2}(\mathbf{K}_e - \mathbf{D}_e)\mathbf{D}_e^{-1/2}$ and $\overline{\mathbf{D}}_e$ denotes the diagonal matrix of $\overline{\mathbf{L}}_e$; N_{elem} represents the total number of elements. From the perspective of programming implementation, it is not necessary to compute the inverse matrix of matrix $\mathbf{C}$, and a detailed algorithm to perform the $\overline{\mathbf{R}}_{k+1} = \mathbf{C}^{-1}\mathbf{U}_{k+1}$ calculation in Eq. (21) can be found in the work of Gullerud and Dodds (2001). Numerical computations show that for 3D hydraulic fracturing simulation, with the same numerical accuracy, the HW preconditioner can reduce the total number of iterations by over 50 % compared to the diagonal preconditioner.

4. Verification and numerical examples

This section validates and shows the capacities of the established numerical model through several examples. The first example simulates regular crossing fractures to verify the enrichment strategy for intersecting fractures proposed in Section 2.2. The second example employs a penny-shaped hydraulic fracturing case to demonstrate the correctness and efficiency of the dual-layer Newton-Raphson iteration scheme proposed in Section 3.5 for the fluid–structure coupling model. The third example is used to validate the contact algorithm for compressive-shear natural fractures described in Section 3.3. The fourth example simulates the interaction between a HF and a NF and compares the simulation results with experimental results. Furthermore, in the final example, the proposed model is utilized to simulate the propagation of multiple fractures within a horizontal well considering the presence of randomly generated natural fractures. It should be noted that in examples presented in Sections 4.3–4.5, the contact iteration calculation is performed using the penalty method (Khoei, 2015) within the inner iteration of the dual-layer Newton-Raphson iteration (Fig. 9).

All examples are performed using an in-house Fortran program PhiPsi (*https://www.phipsi.top*). It is noteworthy that all input files, including the keywords file (**.kpp*) that controls the simulation process, can be accessed from GitHub (*https://github.com/PhiPsi-Software/paper_numerical_examples_1*).

4.1. Regular crossing fractures

To verify the enrichment strategy for intersecting fractures and show the robustness of the proposed model, a cube is taken as the verification model as shown in Fig. 10. As stated in the introduction, the fluid exchange between fractures has not been considered in this paper. Thus, uniform fluid pressures will be applied to all fractures. The choice of non-fluid-exchanging crossing fractures serves as a simplified yet necessary test case to assess the ability of the model to capture fracture apertures and interactions between fractures. The elastic modulus E of the model is 20 GPa, and the Poisson's ratio ν is 0.2. For the geometric model shown in Fig. 10 (a), there are two intersecting rectangle fractures with fixed boundaries on all four sides and free boundaries on the top and bottom. For the model depicted in Fig. 10 (b), there are three intersecting rectangular fractures, and all six faces of the cube have fixed boundaries. Fractures 1–3 are subjected to uniform fluid pressures P_1, P_2, and P_3, respectively. The size of fractures 1 and 2 in Fig. 10 (a) is 8 m by 21 m, and all three fractures in Fig. 10 (b) have dimensions of 8 m by 8 m. Displacement fields are computed and compared with the results obtained using the commercial software ANSYS. Four cases are considered in this example, as listed in Table 1.

The comparison of the maximum value of the displacement vector sum ($u_{eqv} = \sqrt{u_x^2 + u_y^2 + u_z^2}$) with ANSYS for the four cases is given in Table 2. It can be observed that the error of all cases compared to ANSYS is less than 1 %. The equivalent displacement contour plots at the top surface plane ($Z = 21$ m) of case 1 are presented in Fig. 11. In case 1, since the ANSYS model is discretized using tetrahedral elements, the

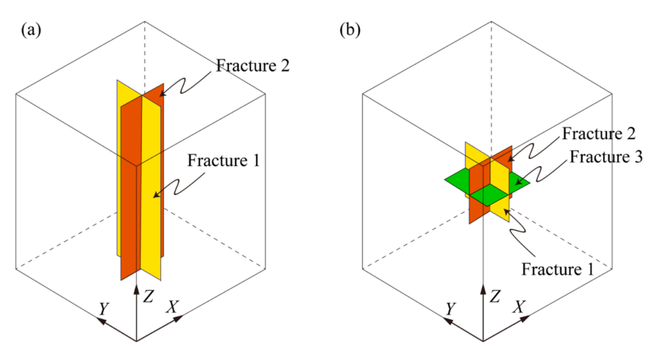

Fig. 10. Geometric models of Example 1. (a) Two fractures in a cube with a side length of 21 m and (b) three fractures in a cube with dimensions 20 m on each side.

Table 1
Parameters of four different cases in Example 1.

Parameter	Case 1	Case 2	Case 3	Case 4
Geometric model	Fig. 10 (a)	Fig. 10 (a)	Fig. 10 (b)	Fig. 10 (b)
P_1 (MPa)	10	10	10	5
P_2 (MPa)	10	5	10	10
P_3 (MPa)	/	/	10	15
N_{elem} in PhiPsi (ten thousand)	4.29	4.29	9.11	9.11
N_{elem} in ANSYS (ten thousand)	21.3	21.3	33.04	33.04

Table 2
The maximum value of the displacement vector sum of all cases.

Software	Case 1	Case 2	Case 3	Case 4
ANSYS (mm)	3.864	3.534	2.514	3.950
PhiPsi (mm)	3.892	3.500	2.499	3.951
Relative error	0.72 %	0.96 %	0.60 %	0.03 %

total number of elements in the ANSYS model is approximately five times that of the PhiPsi model. In addition, the CPU time to solve the linear equation system in the ANSYS model and the PhiPsi model are 9 s and 3 s, respectively, in case 1. From Fig. 11, it can be seen that the ANSYS model has a refined mesh near the fracture tips, while the PhiPsi model utilizes a regular sparser mesh independent of the fractures. Even so, the resulting equivalent displacement contour plots are almost identical between two models. The aperture contour plot for case 3, as displayed in Fig. 12 (a), exhibits that the apertures of all three fractures are identical since all three fractures undergo the same fluid pressure. In case 4, fracture 3 has the highest fluid pressure, resulting in the largest aperture, as depicted in Fig. 12 (b). Since the contact interaction between surfaces of fracture has not been considered in this example, the aperture of fracture 1 with the lowest fluid pressure is negative under the strong influence of higher pressure from fractures 2 and 3. The comparison of displacement contour at the cross-sections for case 4 is shown in Fig. 13, from which it can be observed that results from PhiPsi and ANSYS are consistent in terms of both displacement distribution and numerical range. The examples given in this section are sufficient to demonstrate that the proposed XFEM element enrichment strategy for intersecting fractures in this study is effective and reliable. All data for this validation example, including the ANSYS APDL script, can be obtained from the provided GitHub link.

To further investigate the robustness of the proposed model, case 1 with five different mesh sizes is simulated. The number of element divisions for each edge of the cubic model are 15, 25, 35, 45, and 55. Thus, the element sizes are around 0.714 m, 1.19 m, 1.667 m (the mesh size adopted in the above simulation of Case 1), 2.143 m, and 2.619 m,

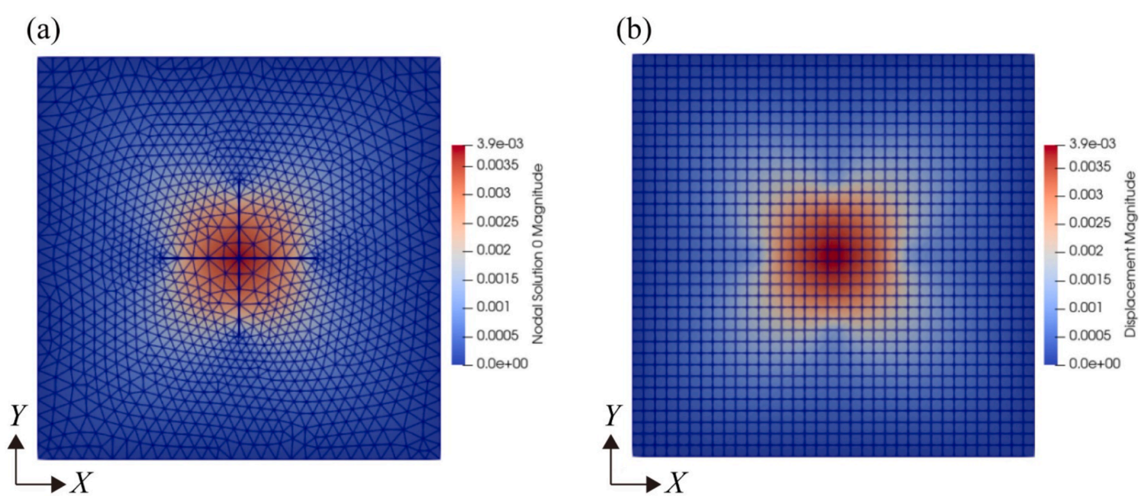

Fig. 11. Comparison of equivalent displacement contours (post-processed using Paraview) at the top surface plane ($Z = 21$ m) of case 1. (a) Results of ANSYS and (b) results of PhiPsi.

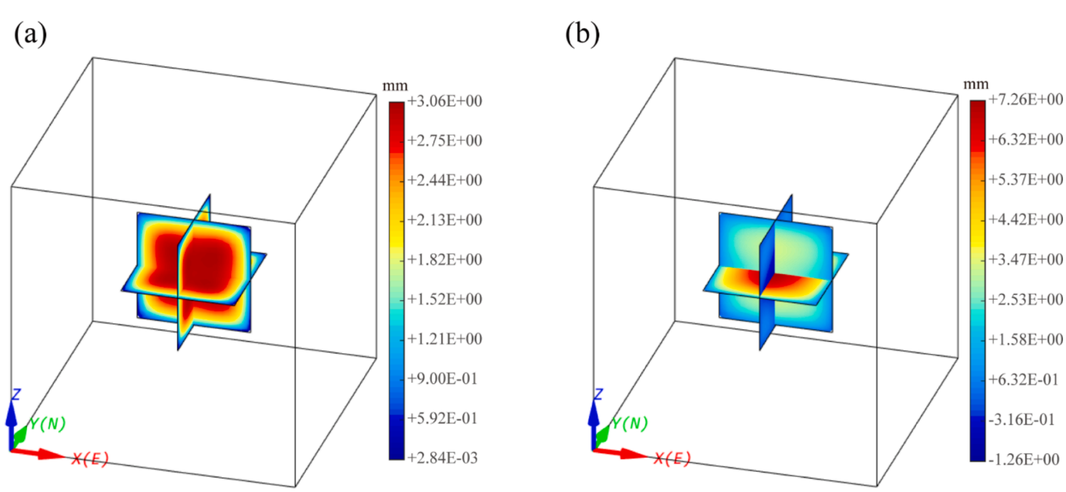

Fig. 12. Fracture aperture contour plots (post-processed using Matlab). (a) Case 3 and (b) case 4.

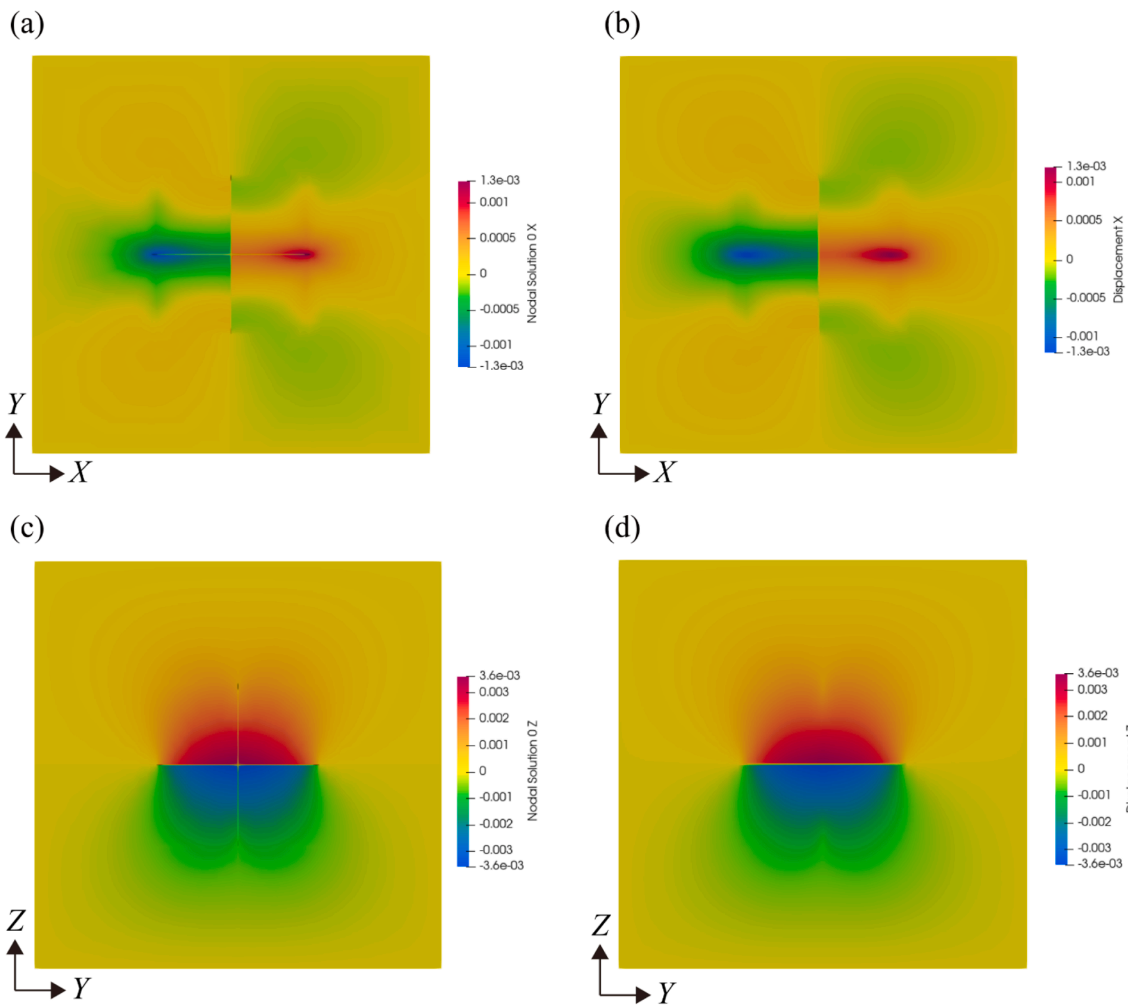

Fig. 13. Comparison of displacement contours (post-processed using Paraview) at the cross-section for case 4. Displacement contour in the *X* direction obtained from (a) ANSYS and (b) PhiPsi at the $Z = 10$ m plane, and displacement contour in the *Z* direction obtained from (c) ANSYS and (d) PhiPsi at the $X = 10$ m plane.

respectively. Besides, the total number of elements are 3,375, 15,625, 42,875, 91,125, and 16,6375, respectively. The relative error between PhiPsi results and ANSYS results of the maximum value of the displacement vector sum for case 1 with different mesh densities is presented in Fig. 14. Specifically, the relative error for the cases with increasing mesh density is 7.14 %, 2.95 %, 0.72 %, 0.41 %, and 0.2 %, respectively, and the time to solve the linear system of equations is 0.3 s, 1.1 s, 3.3 s, 8.2 s, and 18.4 s, respectively. It can be seen that the relative error drops rapidly when the grid density increases. When the number of element divisions is taken as 35, the relative error is 0.72 %, indicating that the XFEM is able to achieve acceptable accuracy without using a very dense mesh in this example. Of course, refining the mesh can further reduce the error, but it will significantly increase the time required to solve the system of linear equations. For instance, when the number of elements is increased to 45, the error further decreases to 0.41 %, but the computation time dramatically rises by 148 %. Therefore, it is crucial to select an appropriate mesh density while ensuring precision, in order to avoid heavy computational burden. In practice, the choice of mesh density is unrelated to the model size; rather, it is directly related to the ratio of initial crack size to model size, and mainly depends on whether the mesh is of sufficient resolution to effectively capture the initial cracks. Generally, the smaller the ratio of initial crack size to model size, the denser the mesh division should be.

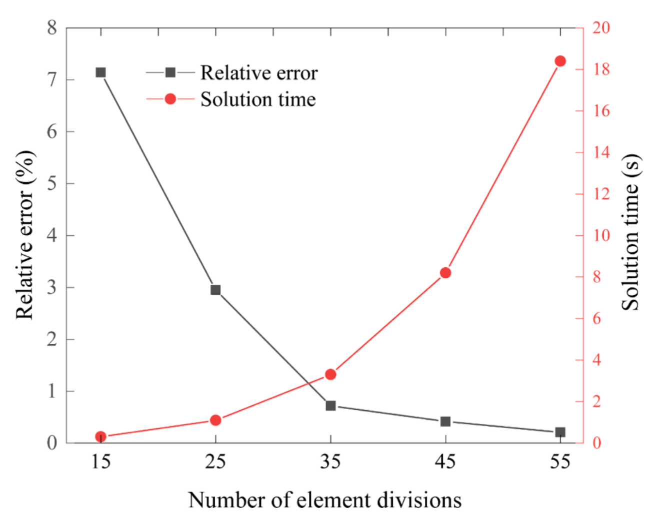

Fig. 14. Relative error of the maximum value of the displacement vector sum for case 1 with different mesh densities. The time to solve the linear system of equations is also shown in this figure.

4.2. Propagation of penny-shaped pressurized fracture

In this section, the propagation of a penny-shaped fracture will be simulated to verify the dual-layer Newton-Raphson iteration scheme for solving the fluid–structure coupling problem. As shown in Fig. 15, a penny-shaped fracture is centrally located in a model of size 200 × 200 × 200 m. All boundaries are supported with rollers. The elasticity modulus E, Poisson's ratio ν, and fracture toughness K_{Ic} of the rock medium are taken as 17 GPa, 0.25, and 2 MPa·m$^{1/2}$, respectively. The flow rate Q_0 and viscosity μ of the injected fluid are set to 0.01 m^3/s, and 0.0001 Pa·s, respectively. The maximum step length for crack propagation is 0.5 m (Shi and Liu, 2021). The model consists of 34,496 hexahedral elements with a refined mesh in the region around the fracture. Details of the finite element model can be found in the linked GitHub repository. For a toughness-dominated penny-shaped hydraulic fracture without fluid leak-off, the asymptotic analytical solutions can be written as (Savitski and Detournay, 2002):

$$R(t) = \mathscr{L}[0.8546 - 0.7349\mathscr{M}\mu'] \tag{24}$$

$$p(\rho, t) = \mathscr{E}E'\left\{0.3004 + \mathscr{M}\left[0.638 - 0.5697\ln\rho + 0.3418\ln\left(1-\rho^2\right)\right]\right\} \tag{25}$$

where t represents the pumping time, $R(t)$ denotes the radius of the evolving fracture at time instant t, $p(\rho, t)$ is the fluid pressure at a point with a distance of r from the fracture center, and $\rho = r/R$. Besides, $E' = E/\left(1-\nu^2\right)$, $\mu' = 12\mu$, $K' = 4\sqrt{2/\pi}K_{Ic}$, $\mathscr{M} = \mu'\left(\frac{Q_0^3E'^{13}}{K'^{18}t^2}\right)^{\frac{1}{5}}$, $\mathscr{E} = \left(\frac{K'^6}{E'^6Q_0t}\right)^{\frac{1}{5}}$, and $\mathscr{L} = \left(\frac{Q_0^2E'^2t^2}{K'^2}\right)^{\frac{1}{5}}$. A Matlab script to calculate the analytical solutions can be found in the GitHub repository.

The variations of fracture radius and fluid pressure with time are shown in Fig. 16 and Fig. 17, respectively. The comparison reveals a satisfactory alignment between the numerical findings and the theoretical predictions. In addition, during the dual-layer Newton-Raphson iteration process described in Section 3.5, both the inner iteration for fluid pressure and the outer time step iteration converge within a maximum of 2 iterations. Accordingly, it can be concluded that the iterative solution algorithm is capable of accurately simulating the propagation of fractures under uniformly distributed fluid pressure with a fast convergence speed.

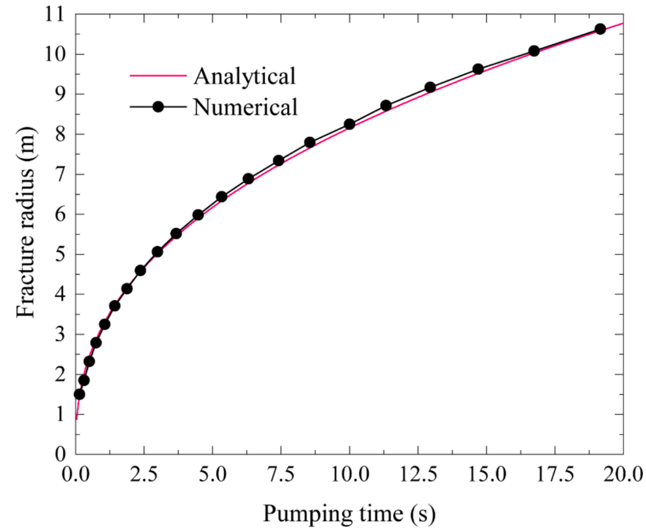

Fig. 16. Comparison of fracture radius with the analytical solution.

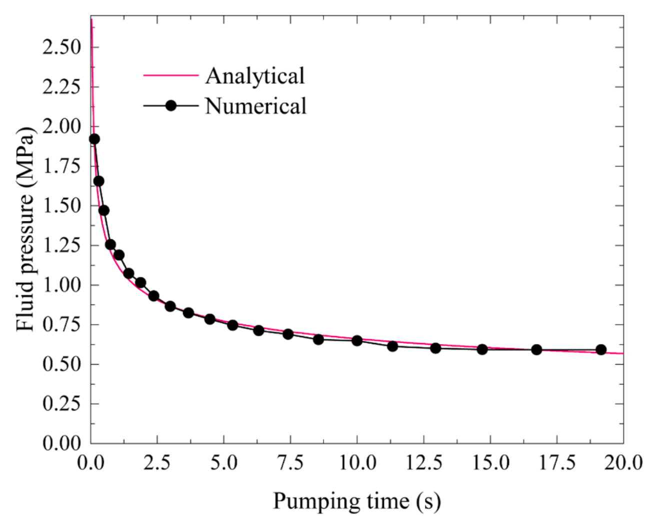

Fig. 17. Comparison of fluid pressure with the analytical solution.

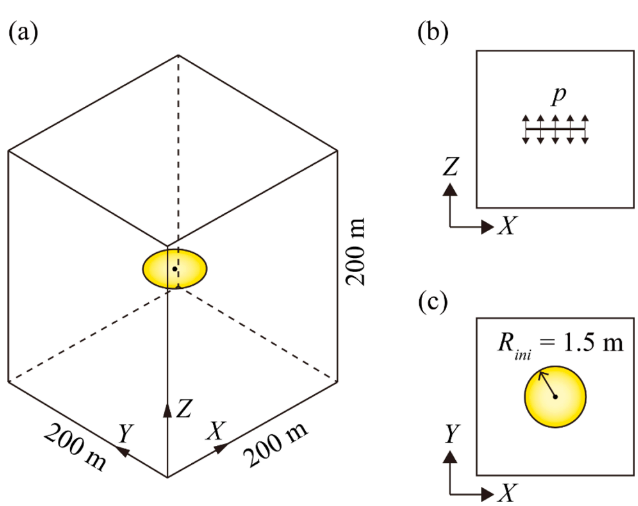

Fig. 15. Schematic representation of a cubic domain with a penny-shaped fracture inside. (a) The geometric model, (b) the front view, and (c) the top view. The initial radius R_{ini} of the fracture is 1.5 m. In figures (b) and (c), the fracture is zoomed in.

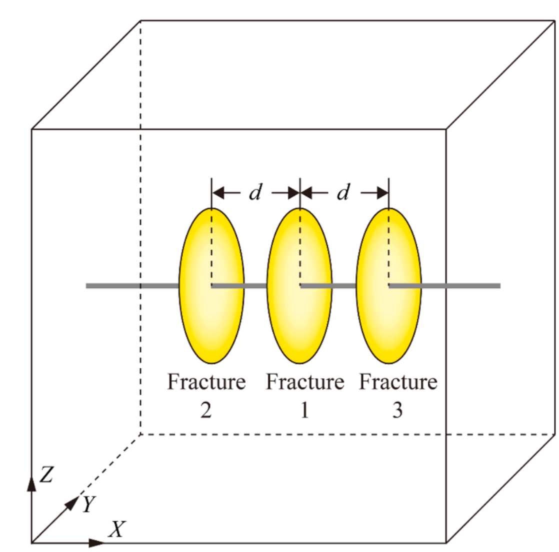

Fig. 18. Illustration of a cubic model containing three parallel penny-shaped fractures.

4.3. Contact of fractures

This section is going to investigate the contact algorithm described in Section 3.3. As shown in Fig. 18, three penny-shaped fractures with equal spacing $d = 20$ m are distributed perpendicular to the X-axis of a cubic model. Fracture 1 is positioned at the center of the model with a side length of 100 m, and all three fractures have a radius of 20 m. The elastic modulus E is 20 GPa, and the Poisson's ratio ν is 0.2. The fluid pressure applied on hydraulic fracture 1 is 10 MPa, while fractures 2 and 3 are natural fractures. All boundaries of the model are supported with rollers. The model is evenly discretized into 51 segments along the X-axis direction and 31 segments in other directions, resulting in a total of 49,001 hexahedral elements. Three cases are investigated in this section: Case 1 does not consider the contact effect between surfaces of NFs; Case 2 determines the contact state using the penalty method (Khoei, 2015) by performing Newton-Raphson iteration; and case 3 utilizes the newly proposed contact algorithm in light of the penalty function method to perform the calculation.

The fracture aperture contour plots obtained from the three cases are shown in Fig. 19, and details of the simulation results are summarized in Table 3. The maximum aperture of fracture 1 is 32.491 mm in case 1 where no contact resistances are considered. Due to the stress shadow effect caused by fracture 1, fractures 2 and 3 have distinct negative apertures (−1.327 mm), which clearly contradicts the actual situation. In case 2, after two Newton-Raphson iterations (Shi et al., 2017), the final maximum apertures of fracture 1 and fractures 2 and 3 are 24.171 mm and 0.000485 mm, respectively. The consumed CPU time is 54 s using an AMD 7950X processor. In case 3, the obtained maximum aperture of fracture 1 is 24.244 mm with a tiny relative error of 0.3 % compared to case 2. Because the contact algorithm proposed in this paper does not require iterative calculations, the elapsed time is 19 s, which is only 35.2 % of the time taken in case 2 and is nearly the same as in case 1. Besides, the maximum aperture of fractures 2 and 3 is close to zero and is approximately 0.002 mm, which is sufficiently accurate for hydraulic fracturing simulations. The examples in this section demonstrate that the simple contact calculation method proposed in this paper can effectively simulate natural fractures to avoid unrealistic negative apertures with both high computational efficiency and reliable simulation accuracy. Finally, it should be emphasized that, for NFs that are approached, intersected, or activated by hydraulic fractures, the Newton-Raphson iterative calculation method is still employed in this paper to accurately determine the sliding state between surfaces of NFs.

4.4. Interaction between a hydraulic fracture and a natural fracture

In this section, we will numerically investigate the interaction between a HF and a pre-existing NF, and the simulation results will be compared with the experimental findings reported by Blanton (1982).

Table 3
Details of simulation results of all cases.

Item	Case 1	Case 2	Case 3
Maximum aperture of fracture 1 (mm)	32.491	24.171	24.244
Maximum aperture of fracture 2 (mm)	−1.327	0.000485	0.001926
Maximum aperture of fracture 3 (mm)	−1.327	0.000485	0.001926
Elapsed CPU time (s)	18	54	19

As shown in Fig. 20, a natural fracture perpendicular to the X-Y plane is located within a cubic model of side length 0.5 m. An initial hydraulic fracture of radius 0.02 m emerged at the pumping point coincides with the model center. The stresses applied in the X, Y, and Z directions are represented by σ_H, σ_h, and σ_v, respectively. It is assumed that the HF propagates in a direction orthogonal to the minimum principal stress. The left ($X = 0$), the front ($Y = 0$), and the bottom ($Z = 0$) faces of the model are supported with rollers. As depicted in Fig. 20 (b), the angle between the NF plane and the X-axis is represented by β, and the distance d between the injection point and the center of the NF is taken as 0.035 m. The material is linear elastic with elastic modulus $E = 10$ GPa, the Poisson's ratio $\nu = 0.22$, and fracture toughness $K_{Ic} = 2$ MPa·m$^{1/2}$. The injection rate of the fracturing fluid is 8.2e-7 m^3/s (i.e., 0.05 cubic inch/s). The cohesion, the friction angle, and the fracture toughness of the NF are 0.01 MPa, 37°, and 1.5 MPa·m$^{1/2}$, respectively. The maximum step length for crack propagation is taken as 0.01 m. The model is evenly discretized into 51 segments along all three directions, resulting in a total of 132,651 (i.e., 51^3) hexahedral elements. As detailed in Table 4, we consider four different scenarios corresponding to the confining pressures of experimental cases CT-4, CT-8, CT-20, and CT-22 reported in the reference (Blanton, 1982).

The interaction modes obtained from the simulation and the experiments are listed in Table 5. It can be found that the proposed methodology predicts interaction patterns in agreement with the experiments. The simulated fracture interaction patterns are presented in Fig. 21. For the case CT-4, the deferential stress in the horizontal direction is 2 MPa, and fluid pressure driving the expansion of the hydraulic fracture is greater than the normal compressive stress of value 11.5 MPa acting on the NF. Therefore, as shown in Fig. 21 (a), the natural fracture opens and propagates under the action of fluid pressure. Furthermore, due to the weak strength of the NF, the NF propagates faster and has a wider aperture compared to the HF. The displacement contours in the X and Y directions at the center section plane ($Z = 0.25$ m) of the model are presented in Fig. 22. From this figure, it can be observed that the growth of the NF is asymmetric on both sides of the intersection point and the NF primarily propagates along the lower side ($Y < 0.25$ m). For the case CT-8, the normal compressive stress acting on the NF is 16.25 MPa. Additionally, the minimum principal stress σ_h is 5 MPa. Consequently, compared to CT-4, a much lower fluid pressure is required to sustain the propagation of the HF. Nevertheless, the

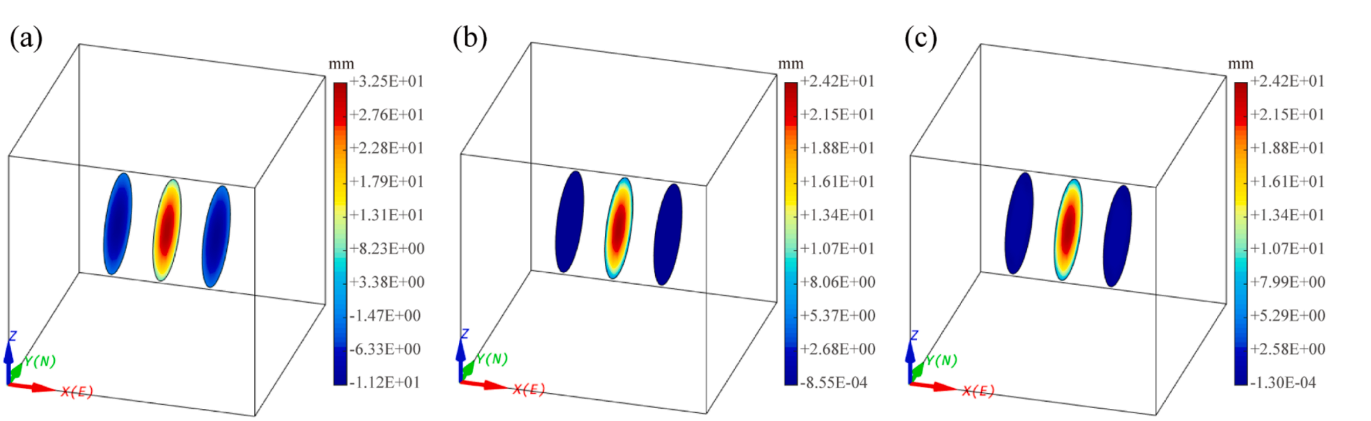

Fig. 19. Contours of fracture aperture. (a) Case 1, (b) case 2, and (c) case 3.

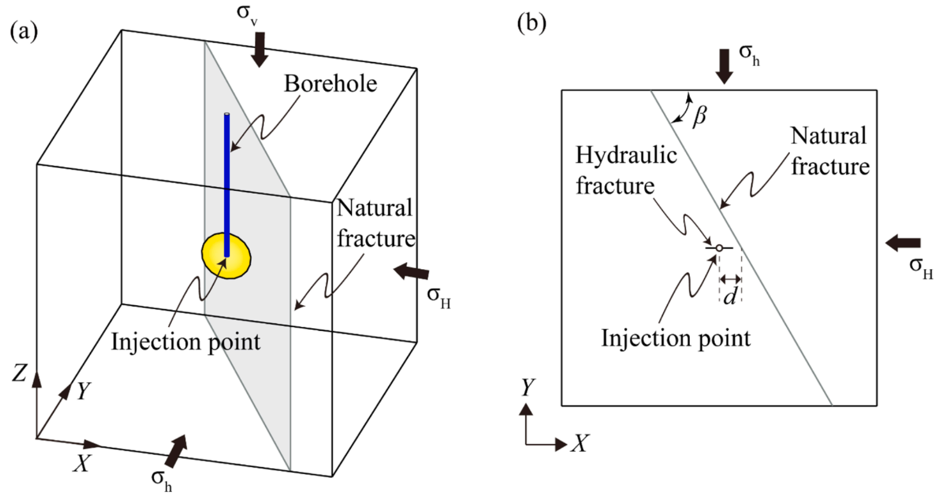

Fig. 20. Schematic representation of a hydraulic fracture and a natural fracture in a cubic model. (a) The oblique view and (b) the top view.

Table 4
Experimental cases selected from Blanton (Blanton, 1982).

Test	β (degree)	σ_H (MPa)	σ_h (MPa)	σ_v (MPa)
CT-4	60	12.0	10.0	20.0
CT-8	60	20.0	5.0	20.0
CT-20	90	14.0	5.0	20.0
CT-22	45	10.0	5.0	20.0

Table 5
Comparison of the fracture interaction modes between experiments and simulation.

Test	Simulation results	Numerical results
CT-4	Opening	Opening
CT-8	Crossing	Crossing
CT-20	Crossing	Crossing
CT-22	Opening	Opening

magnitude of this low fluid pressure significantly falls beneath the normal compressive stress acting on the surfaces of the NF. As a result, the HF crosses the NF while the NF remains closed throughout the simulation, as evident in Fig. 21 (b). For the case CT-20, the normal compressive stress acting on the NF is 14 MPa and the minimum principal stress σ_h is 5 MPa. Therefore, just like CT-8, the HF crosses the NF without activating it, as shown in Fig. 21 (c). For the case CT-22, since the fluid pressure is greater than the normal compressive stress (7.5 MPa) acting on the NF, the NF opens, as shown in Fig. 21 (d).

The simulated interaction types agree with the theoretical analysis and have been confirmed by experimental observations, indicating that the proposed model can predict the interactive behavior between the HF and the NF.

4.5. Multiple-fracture propagation in a horizontal well

In this section, the established numerical model will be ultimately adopted to predict the propagation of three initial hydraulic fractures in a horizontal well. As shown in Fig. 23, a total number of 150 pre-existing natural fractures are randomly distributed inside a cubic model with an edge length of 250 m. All initial natural fractures are described using spatial squares with an average edge length of 35 m. Considering the extreme randomness of the natural fractures, the edge length of squares fluctuates within a range of 10 m following a Gaussian distribution (i.e., the actual edge length ranging from 30 to 40 m) in this example. Besides, the average normal vector of the squares is (1, 0, 1) with a fluctuation angle of 10 degrees in the normal direction (i.e., the angle between the actual normal vector and the average normal vector ranging from −5 to 5 degrees). The horizontal well penetrates through the model along the *X*-axis direction and coincides with the symmetry axis of the model. As illustrated in Fig. 23 (b), three initial HFs of diameter 35 m are positioned centrally on the horizontal well with a gap $d = 22.5$ m between adjacent HFs. All boundaries of the model are fixed with roller constraints. The in-situ stresses in *X* ,*Y*, and *Z* directions are respectively set to 8 MPa, 9 MPa, and 10 MPa. The elastic modulus *E*, the Poisson's ratio ν, and the fracture toughness K_{Ic} of the rock media are taken as 20 GPa, 0.2, and 2 MPa·m$^{1/2}$, respectively. The fluid injection rate is 0.01 m^3/s. The cohesion, the friction angle, and the fracture toughness of the NF are 0.1 MPa, 37°, and 1.0 MPa·m$^{1/2}$, respectively. The maximum step length for crack propagation is taken as 5 m. The model is discretized with 91,125 (i.e., 45ˆ3) hexahedral elements of the same size. The simulation stops when the injection time reaches 60 min.

The consumed CPU time for this simulation is 276 min using an AMD 7950X processor. The final obtained fracture morphology is presented in Fig. 24 in which several NFs are activated and significantly influence the propagation of HFs. From Fig. 24 (b) it can be observed that the HF 2 grows in a non-planar manner and forms an asymmetric elliptical shape. Fig. 25 and Fig. 26 present respectively the evolution of fracture apertures and displacement contours at the center section plane ($Y = 125$ m) at time instants $t = 174.7$ s, 708.7 s, and 3600 s. By comparing figures (a) and (b), it can be observed that HF 1 experiences hindered growth due to the stress shadow effect from HFs 2 and 3. Consequently, it exhibits the minimum fracture aperture and size. From figures (c), it can be seen that, compared to HFs 2 and 3, the propagation length of HF 1 is relatively small during the subsequent fracturing process. Since the minimum in-situ stress is oriented along the *X*-axis direction, which happens to be perpendicular to the initial hydraulic fracture plane, the propagation of activated NFs with an average normal vector of (1, 0, 1) does not play the dominant role, just as shown in the presented figures. The simulation results are consistent with the theoretical predictions based on stress field analysis, indicating that the numerical computational model established in this study possesses the capability to simulate complex non-planar hydraulic fracturing three-dimensional.

5. Conclusions

The research on two-dimensional hydraulic fracturing simulation using the XFEM has gradually matured over the past decade. However, when it comes to three-dimensional simulation, there are still several key challenges to be overcome, and one of them is the simulation of complex intersecting fractures, which must be fully addressed before

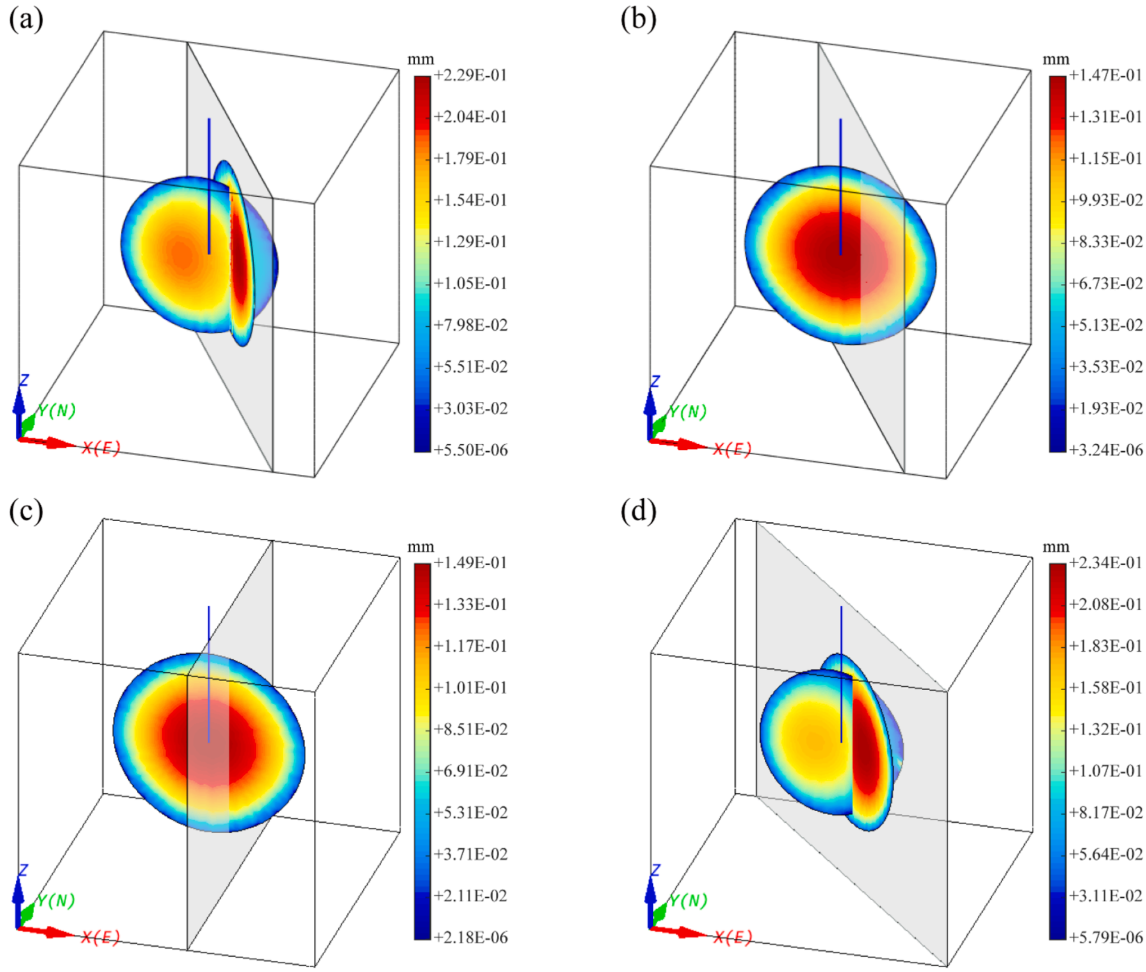

Fig. 21. Fracture interaction patterns and fracture apertures obtained from numerical solutions. (a) The CT-4 test, (b) the CT-8 test, (c) the CT-20 test, and (d) the CT-22 test.

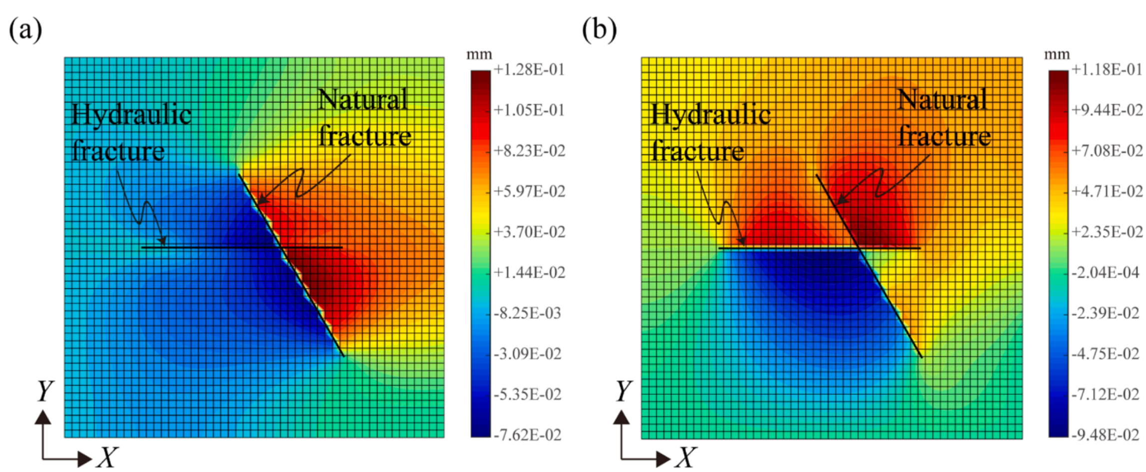

Fig. 22. The displacement contours at the center section plane (Z = 0.25 m) of the CT-4 test. (a) Displacement in the X direction, and (b) displacement in the Y direction.

achieving large-scale hydraulic fracturing simulations of practical engineering value. To this end, this study extends our previous work (Shi and Liu, 2021; Shi et al., 2022b), and establishes, for the first time, a comprehensive simulation strategy for 3D non-planar crossing fractures based on the XFEM. The proposed integration algorithm for enriched elements efficiently resolves the problem of stiffness matrix singularity caused by the complex intersection of fractures. Additionally, it eliminates the requirement for intricate geometric operations like partitioning enriched elements into tetrahedra. Consequently, in theory, it is applicable to simulations involving any number of intersecting fractures, laying a crucial foundation for complex fracturing scenarios. Due to the presence of numerous NFs in real underground environments, a

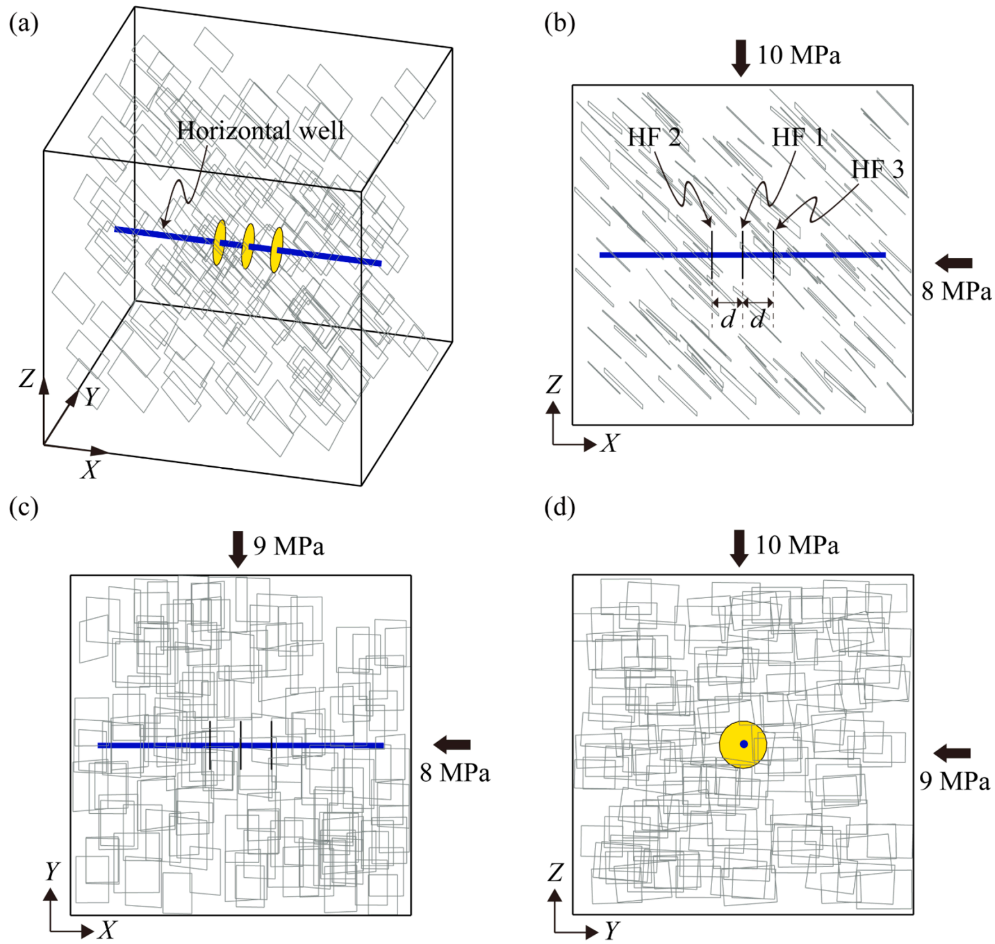

Fig. 23. Schematic diagram of initial hydraulic fractures along a horizontal well in a cubic model in the presence of pre-existing natural fractures represented by gray squares. (a) The oblique view, (b) the front view, (c) the top view, and (d) the right-side view.

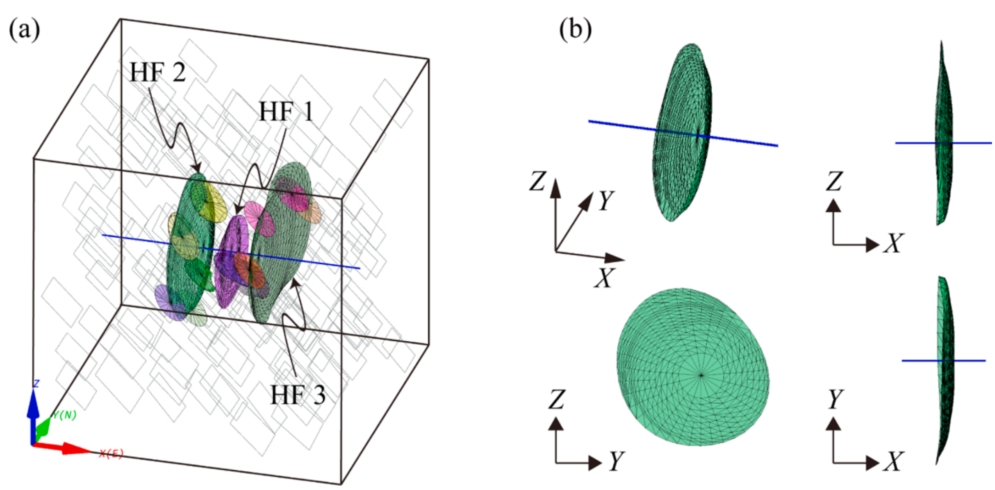

Fig. 24. The final obtained fracture morphology described using spatial triangles. (a) The overall fracture morphology and (b) hydraulic fracture 2 in different views.

contact algorithm in the absence of iteration procedures based on the penalty function method is innovatively proposed to simulate NFs that are not hydraulically connected. After given the fracture propagation and interaction criteria, a Taubin algorithm is introduced to smooth the front of fracture surfaces and eliminate outliers. Afterwards, a dual-layer Newton-Raphson iteration scheme is proposed to maintain the quasi-static fracture propagation criterion and mass conservation law during the fluid–structure coupling calculation. Moreover, the linear equation systems are solved using a PCG solver with a Hughes-Winget preconditioner in an element-by-element manner, and thus the assembly of the global stiffness matrix can be completely avoided.

Several examples are presented to verify and validate key ingredients of the proposed model including the element enrichment strategy and integration algorithm for intersecting fractures, the dual-layer Newton-Raphson iteration scheme, the contact algorithm for compressive-shear natural fractures, as well as the fracture propagation model. The last

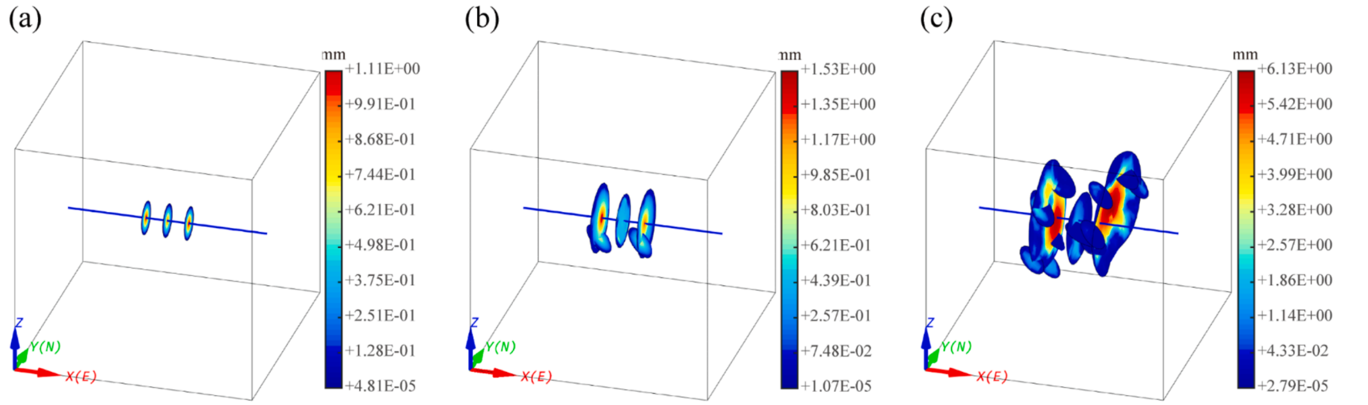

Fig. 25. Contours of fracture aperture. (a) $t = 174.7$ s, (b) $t = 708.7$ s, and (c) $t = 3600$ s. Natural fractures that are not activated are not shown in this figure.

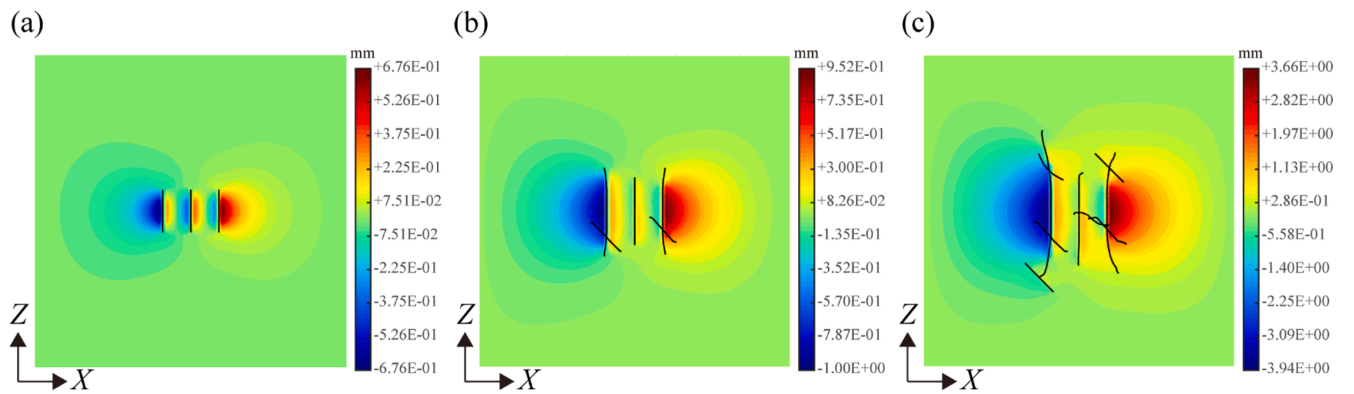

Fig. 26. The displacement contours at the center section plane ($Y = 125$ m) of the model. (a) $t = 174.7$ s, (b) $t = 708.7$ s, and (c) $t = 3600$ s.

example simulates the multi-fracture propagation of fractures in a horizontal well in the presence of 150 randomly generated natural fractures, and good agreements between the XFEM and desired solutions are observed, demonstrating that the proposed model is able to efficiently simulate the propagation and intersection of fractures in complex nonplanar 3-D shapes. All input files of numerical examples as well as the PhiPsi executable file can be found in the linked GitHub repository, so the interested reader can pursue a particular topic in more depth and perform simulations with other sets of parameters. It should be noted that although the non-uniform fluid pressure distribution within fractures has not been included in this paper, the established algorithms can be easily adapted to more complex viscosity-dominated hydraulic fracturing regimes, which will be addressed in future studies.

CRediT authorship contribution statement

Fang Shi: Writing – original draft, Visualization, Software, Methodology, Investigation, Data curation, Conceptualization. **Chunyang Lin:** Writing – review & editing, Validation.

Declaration of competing interest

The authors declare that they have no known competing financial interests or personal relationships that could have appeared to influence the work reported in this paper.

Data availability

Data will be made available on request.

Acknowledgments

This work was supported by the National Natural Science Foundation of China [Grant No. 51904111].

References

Abdelaziz, A., Ha, J., Li, M., Magsipoc, E., Sun, L., Grasselli, G., 2023. Understanding hydraulic fracture mechanisms: from the laboratory to numerical modelling. Adv. Geo-Energy Res. 7 (1), 66–68.
Adachi, J., Siebrits, E., Peirce, A., Desroches, J., 2007. Computer simulation of hydraulic fractures. Int. J. Rock Mech. Min. Sci. 44 (5), 739–757.
Advani, S.H., Lee, J.K., 1982. Finite element model simulations associated with hydraulic fracturing. SPE-3009-PA 22 (02), 209–218.
Bandis, S.C., Lumsden, A.C., Barton, N.R., 1983. Fundamentals of rock joint deformation. Int. J. Rock Mech. Min. Sci. Geomech. Abstr. 20 (6), 249–268.
Belytschko, T., Black, T., 1999. Elastic crack growth in finite elements with minimal remeshing. Int. J. Numer. Meth. Eng. 45, 601–620.
Blanton, T.L., 1982. An experimental study of interaction between hydraulically induced and pre-existing fractures. In: SPE Unconventional Gas Recovery Symposium. Society of Petroleum Engineers of AIME, Pittsburgh, Pennsylvania.
Chandrupatla, T.R., Belegundu, A.D., Ramesh, T., Ray, C., 2012. Introduction to Finite Elements in Engineering. Prentice Hall, New Jersey.
Chen, B., Barboza, B.R., Sun, Y., Bai, J., Thomas, H.R., Dutko, M., Cottrell, M., Li, C., 2022. A review of hydraulic fracturing simulation. Arch. Comput. Meth. Eng. 19, 1–58.
Chen, B., Yu, T., Natarajan, S., Zhang, Q., Bui, T.Q., 2023. Numerical simulation for quasi-static crack growth and dynamic crack branching by coupled state-based PD and XFEM. Acta Mech. 234, 3605–3622.
Cheng, L., Luo, Z., Yu, Y., Zhao, L., Zhou, C., 2019. Study on the interaction mechanism between hydraulic fracture and natural karst cave with the extended finite element method. Eng. Fract. Mech. 222, 106680.
Cruz, F., Roehl, D., do Amaral Vargas Jr., E., 2018. An XFEM element to model intersections between hydraulic and natural fractures in porous rocks. Int. J. Rock Mech. Min. Sci. 112, 385–397.
Daux, C., Moës, N., Dolbow, J., Sukumar, N., Belytschko, T., 2000. Arbitrary branched and intersecting cracks with the extended finite element method. Int. J. Numer. Meth. Eng. 48 (12), 1741–1760.

Dehghan, A.N., Goshtasbi, K., Ahangari, K., Jin, Y., Bahmani, A., 2017. 3D numerical modeling of the propagation of hydraulic fracture at its intersection with natural (pre-existing) fracture. Rock Mech. Rock Eng. 50, 367–386.
Fu, W., Savitski, A.A., Damjanac, B., Bunger, A.P., 2019. Three-dimensional lattice simulation of hydraulic fracture interaction with natural fractures. Comput. Geotech. 107, 214–234.
Gullerud, A.S., Dodds Jr., R.H., 2001. MPI-based implementation of a PCG solver using an EBE architecture and preconditioner for implicit, 3-D finite element analysis. Comput. Struct. 79, 553–575.
Gupta, P., Duarte, C.A., 2018. Coupled hydromechanical-fracture simulations of nonplanar three-dimensional hydraulic fracture propagation. Int. J. Numer. Anal. Meth. Geomech. 42, 143–180.
Haddad, M., Sepehrnoori, K., 2016. XFEM-based CZM for the simulation of 3D multiple-cluster hydraulic fracturing in quasi-brittle shale formations. Rock Mech. Rock Eng. 49, 4731–4748.
Heider, Y., 2021. A review on phase-field modeling of hydraulic fracturing. Eng. Fract. Mech. 253, 107881.
Hirmand, M., Vahab, M., Khoei, A.R., 2015. An augmented Lagrangian contact formulation for frictional discontinuities with the extended finite element method. Finite Elem. Anal. Des. 107, 28–43.
Hosseini, N., Khoei, A.R., 2020. Numerical simulation of proppant transport and tip screen-out in hydraulic fracturing with the extended finite element method. Int. J. Rock Mech. Min. Sci. 128, 104247.
Jafari, A., Vahab, M., Khalili, N., 2021. Fully coupled XFEM formulation for hydraulic fracturing simulation based on a generalized fluid leak-off model. Comput. Method. Appl. Mech. Eng. 373, 113447.
Jamaloei, B.Y., 2021. A critical review of common models in hydraulic-fracturing simulation: A practical guide for practitioners. Theor. Appl. Fract. Mech. 113, 102937.
Jin, W., Arson, C., 2020. Fluid-driven transition from damage to fracture in anisotropic porous media: a multi-scale XFEM approach. Acta Geotech. 15, 113–144.
Khoei, A.R., 2015. Extended Finite Element Method: Theory and Applications. John Wiley & Sons, London.
Khoei, A.R., Haghighat, E., 2011. Extended finite element modeling of deformable porous media with arbitrary interfaces. App. Math. Model. 35 (11), 5426–5441.
Khoei, A.R., Hirmand, M., Vahab, M., Bazargan, M., 2015. An enriched FEM technique for modeling hydraulically driven cohesive fracture propagation in impermeable media with frictional natural faults: numerical and experimental investigations. Int. J. Numer. Meth. Eng. 104 (6), 439–468.
Khoei, A.R., Vahab, M., Hirmand, M., 2016. Modeling the interaction between fluid-driven fracture and natural fault using an enriched-FEM technique. Int. J. Fract. 197, 1–24.
Khoei, A.R., Hirmand, M., Vahab, M., Hirmand, M., 2018. An enriched–FEM technique for numerical simulation of interacting discontinuities in naturally fractured porous media. Comput. Methods Appl. Mech. Eng. 331, 197–231.
Lecampion, B., 2009. An extended finite element method for hydraulic fracture problems. Commun. Numer. Methods Eng. 25 (2), 121–133.
Lecampion, B., Bunger, A., Zhang, X., 2018. Numerical methods for hydraulic fracture propagation: a review of recent trends. J. Nat. Gas Sci. Eng. 49, 66–83.
Luo, Z., Cheng, L., Zhao, L., Xie, Y., 2022. Numerical simulation and analysis of thermo-hydro-mechanical behaviors of hydraulic fracturing in naturally fractured formation using a THM-XFEM coupling model. J. Nat. Gas Sci. Eng. 103, 104657.
Maulianda, B., Savitri, C.D., Prakasan, A., Atdayev, E., Yan, T.W., Yong, Y.K., Elrais, K.A., Barati, R., 2020. Recent comprehensive review for extended finite element method (XFEM) based on hydraulic fracturing models for unconventional hydrocarbon reservoirs. J. Pet. Explor. Prod. Technol. 10, 3319–3331.
Moës, N., Dolbow, J., Belytschko, T., 1999. A finite element method for crack growth without remeshing. Int. J. Numer. Meth. Eng. 46 (1), 131–150.
Mukhtar, F.M., Shauer, N., Duarte, C.A., 2022. Propagation mechanisms and parametric influence in multiple interacting hydraulic fractures: a 3-D G/XFEM hydro-mechanical modeling. Int. J. Numer. Anal. Meth. Geomech. 46, 2033–2059.
Ni, T., Pesavento, F., Zaccariotto, M., Galvanetto, U., Zhu, Q.-Z., Schrefler, B.A., 2020. Hybrid FEM and peridynamic simulation of hydraulic fracture propagation in saturated porous media. Comput. Method. Appl. Mech. Eng. 366, 113101.
Parchei-Esfahani, M., Gee, B., Gracie, R., 2020. Dynamic hydraulic stimulation and fracturing from a wellbore using pressure pulsing. Eng. Fract. Mech. 235, 107152.
Paul, B., Faivre, M., Massin, P., Giot, R., Colombo, D., Golfier, F., Martin, A., 2018. 3D coupled HM–XFEM modeling with cohesive zone model and applications to non planar hydraulic fracture propagation and multiple hydraulic fractures interference. Comput. Method. Appl. Mech. Eng. 342, 321–353.
Qin, M., Yang, D., 2023. Numerical investigation of hydraulic fracture height growth in layered rock based on peridynamics. Theor. Appl. Fract. Mech. 125, 103885.
Roth, S.-N., Léger, P., Soulaïmani, A., 2020a. Fully-coupled hydro-mechanical cracking using XFEM in 3D for application to complex flow in discontinuities including drainage system. Comput. Method. Appl. Mech. Eng. 370, 113282.
Roth, S.-N., Léger, P., Soulaïmani, A., 2020b. Strongly coupled XFEM formulation for non-planar three-dimensional simulation of hydraulic fracturing with emphasis on concrete dams. Comput. Method. Appl. Mech. Eng. 363, 112899.
Sanchez, E.C.M., Cordero, J.A.R., Roehl, D., 2020. Numerical simulation of three-dimensional fracture interaction. Comput. Geotech. 122, 103528.
Savitski, A.A., Detournay, E., 2002. Propagation of a penny-shaped fluid-driven fracture in an impermeable rock: asymptotic solutions. Int. J. Solids Struct. 39, 6311–6337.
Schöllmann, M., Richard, H.A., Kullmer, G., Fulland, M., 2002. A new criterion for the prediction of crack development in multiaxially loaded structures. Int. J. Fract. 117, 129–141.
Shauer, N., Duarte, C.A., 2022. A three-dimensional Generalized Finite Element Method for simultaneous propagation of multiple hydraulic fractures from a wellbore. Eng. Fract. Mech. 265, 108360.
Shi, F., Liu, J., 2021. A fully coupled hydromechanical XFEM model for the simulation of 3D non-planar fluid-driven fracture propagation. Comput. Geotech. 132, 103971.
Shi, F., Wang, X., Liu, C., Liu, H., Wu, H., 2017. An XFEM-based method with reduction technique for modeling hydraulic fracture propagation in formations containing frictional natural fractures. Eng. Fract. Mech. 173, 64–90.
Shi, F., Wang, D., Li, H., 2022a. An XFEM-based approach for 3D hydraulic fracturing simulation considering crack front segmentation. J. Pet. Sci. Eng. 214, 110518.
Shi, F., Wang, D., Yang, Q., 2022b. An XFEM-based numerical strategy to model three-dimensional fracture propagation regarding crack front segmentation. Theor. Appl. Fract. Mech. 118, 103250.
Smith, I.M., Griffiths, D.V., Margetts, L., 2014. Programming the Finite Element Method. John Wiley & Sons, West Sussex, United Kingdom.
Taleghani, A.D., Gonzalez, M., Shojaei, A., 2016. Overview of numerical models for interactions between hydraulic fractures and natural fractures: challenges and limitations. Comput. Geotech. 71, 361–368.
Taleghani, A.D., Olson, J.E., 2014. How natural fractures could affect hydraulic-fracture geometry. SPE J. 19 (1), 161–171.
Tang, H., Wang, S., Zhang, R., Li, S., Zhang, L., Wu, Y., 2019. Analysis of stress interference among multiple hydraulic fractures using a fully three-dimensional displacement discontinuity method. J. Pet. Sci. Eng. 179, 378–393.
Taubin, G., 1995. Curve and surface smoothing without shrinkage. In: Proceedings of the Fifth International Conference on Computer Vision. IEEE Transactions on Computers, Cambridge, MA, USA.
Vahab, M., Khoei, A.R., Khalili, N., 2019. An X-FEM technique in modeling hydro-fracture interaction with naturally-cemented faults. Eng. Fract. Mech. 212, 269–290.
Wang, C., Huang, Z., Wu, Y.-S., 2020. Coupled numerical approach combining X-FEM and the embedded discrete fracture method for the fluid-driven fracture propagation process in porous media. Int. J. Rock Mech. Min. Sci. 130, 104315.
Yang, P., Zhang, S., Zou, Y., Zhong, A., Yang, F., Zhu, D., Chen, M., 2024. Numerical Simulation of integrated three-dimensional hydraulic fracture propagation and proppant transport in multi-well pad fracturing. Comput. Geotech. 167, 106075.
Zhang, F., Damjanac, B., Maxwell, S., 2019. Investigating hydraulic fracturing complexity in naturally fractured rock masses using fully coupled multiscale numerical modeling. Rock Mech. Rock Eng. 5137–5160.
Zhang, J., Yu, H., Xu, W., Lv, C., Micheal, M., Shi, F., Wu, H., 2020. A hybrid numerical approach for hydraulic fracturing in a naturally fractured formation combining the XFEM and phase-field model. Eng. Fract. Mech. 366, 113101.
Zhao, Y., Jiang, H., Rahman, S., Yuan, Y., Zhao, L., Li, J., Ge, J., Li, J., 2019. Three-dimensional representation of discrete fracture matrix model for fractured reservoirs. J. Pet. Sci. Eng. 180, 886–900.
Zheng, S., Manchanda, R., Sharma, M.M., 2019. Development of a fully implicit 3-D geomechanical fracture simulator. J. Pet. Sci. Eng. 179, 758–775.
Zhuang, X., Li, X., Zhou, S., 2023. Transverse penny-shaped hydraulic fracture propagation in naturally-layered rocks under stress boundaries: a 3D phase field modeling. Comput. Geotech. 155, 105205.